Examination of effects of aerosols on a pyroCb and their dependence on fire intensity and aerosol perturbation

Seoung Soo Lee[1], George Kablick III[2,3], Zhanqing Li[2], Chang-Hoon Jung[4], Yong-Sang Choi[5]

[1]Research Foundation, San Jose State University, San Jose, California, USA

[2]Earth System Science Interdisciplinary Center, University of Maryland, College Park, Maryland, USA

[3]US Naval Research Laboratory, Washington, DC, USA

[4]Department of Health Management, Kyungin Women's University, Incheon, South Korea

[5]Department of Environmental Science and Engineering, Ewha Womans University, Seoul, South Korea

Abstract

This study investigates how a pyrocumulonimbus (pyroCb) event influences water vapor concentrations and cirrus cloud properties near the tropopause, specifically focusing on how fire-produced aerosols affect this role via a modeling framework. Results from a case study show that when observed fire intensity is high, there is an insignificant impact of fire-produced aerosols on the convective development of the pyroCb and associated changes in water vapor and the amount of cirrus cloud near the tropopause. However, as fire intensity weakens, effects of aerosols on microphysical variables and processes such as droplet size and autoconversion increase. Modeling results shown herein indicate that aerosol-induced invigoration of convection is significant for pyroCb with weak-intensity fires and associated weak surface heat fluxes. Thus, there is a greater aerosol effect on the transportation of water vapor to the upper troposphere and the production of cirrus cloud with weak-intensity fires, whereas these effects are muted with strong-intensity fires.

1. Introduction

Recent studies (e.g., Pumphrey et al., 2011; Kablick et al., 2018) have shown that pyrocumulonimbus (pyroCbs) can transport significant amounts of water vapor to the upper troposphere and the lower stratosphere (UTLS) and thus may play a role in seasonal UTLS water vapor budgets. Any change in water vapor in the UTLS has an exceptionally strong influence on the global radiation budget and thus Earth's climate (Solomon et al., 2010). PyroCbs involve and control cirrus clouds around their tops that reach the UTLS. Changes in cirrus clouds in the UTLS are known to have a strong influence on the global radiation budget (Solomon et al., 2010). The level of our understanding of impacts of pyroCbs on water vapor and cirrus clouds in the UTLS over the global scale is very low and studies to improve this understanding has been going on (Fromm et al., 2010). However, this paper does not focus on these pyroCb impacts at the global scale. Instead, this paper aims to gain a process-level understanding of mechanisms that control impacts of individual pyroCbs on water vapor and cirrus clouds in the UTLS. The examination of these mechanisms can provide useful information to parameterize interactions among pyroCbs, water vapor and cirrus clouds in climate models. Hence, this examination can contribute to studies that try to improve our understanding of the global-scale impacts of pyroCbs on water vapor and cirrus clouds by using climate models.

By definition, pyroCbs initiate over a fire, and the large surface energy release affects their dynamic, thermodynamic and microphysical development (Fromm et al., 2010; Peterson et al., 2017). The dynamics of these events has been shown to be mostly controlled by fire-induced latent and sensible heat fluxes at and near the surface. However, questions remain about what role the large concentration of cloud condensation nuclei (CCN) contained in smoke has on the vertical development and microphysical properties. Studies (e.g., Rosenfeld et al., 2008; Storer et al., 2010; Tao et al., 2012) have shown that aerosols affect cumulonimbus clouds, and this raises a possibility that fire-generated aerosols affect pyroCb development. As an example of aerosol impacts on cumulonimbus clouds, these studies have demonstrated that increases in aerosol loading can make the size of droplets (i.e., cloud-liquid particles) smaller. Individual aerosol particles act as seeds for the formation of droplets and thus increasing aerosol loading or increasing aerosol

concentrations lead to more droplets formed. More droplets mean more competition among them for available water vapor needed for their condensational growth, and this more competition makes individual droplets smaller (Twomey, 1977; Albrecht, 1989). Aerosol-induced smaller sizes of droplets reduce the efficiency of the growth of cloud-liquid particles to raindrops via autoconversion that is a collection process among cloud-liquid particles for them to grow to be raindrops, given that the efficiency is proportional to the sizes (Pruppacher and Klett, 1978; Rogers and Yau, 1991). This reduced efficiency leads to less cloud liquid converted to rain. More cloud liquid is thus available for transport to places above the freezing level by updrafts. This eventually induces more freezing of cloud liquid, which enhances parcel buoyancy, and this enhancement invigorates updrafts and associated convection (Rosenfeld, 2008).

Compared to the research done on the role played by fire-generated heat fluxes in the development of pyroCbs and their effects on water vapor and cirrus clouds in the UTLS, the research on that role by fire-generated aerosols has been scarce. Motivated by this lack of understanding, this paper focuses on the role by those aerosols in the development of a pyroCb and its effects on water vapor and cirrus clouds in the UTLS. To examine that role, this study extends the previous modeling work that was described in Kablick et al. (2018). That modeling work compared effects of fire-generated heat fluxes on the development of a pyroCb and its impacts on the UTLS water vapor and cirrus clouds to those of fire-generated aerosols. In that comparison, those effects of fire-generated aerosols were shown to be negligible as compared to those effects of heat fluxes. However, aerosol effects on cloud development vary with cloud typical properties such as typical updraft speeds that are determined by environmental conditions (e.g., Khain et al., 2008; Lee et al., 2008; Tao et al., 2012). For the simplicity of the term, in this study, “typical updraft speeds” are referred to as “typical updrafts”. Typical updrafts are determined by environmental instability as represented by convective available potential energy (CAPE). Lee et al. (2008) have shown that different clouds with different typical updrafts, which are due to different CAPE, show different sensitivity of cloud microphysical and thermodynamic development to aerosol concentration. Hence, it is hypothesized that aerosol effects on the pyroCb development and its impacts on the UTLS water vapor and cirrus clouds can vary depending on the intensity of the pyroCb typical updrafts.

Based on this hypothesis, to examine the potential variation of aerosol effects on the pyroCb development and its impacts on the UTLS water vapor and cirrus clouds with the varying typical updrafts of pyroCbs, numerical simulations are performed. These simulations are for a case of a pyroCb which is identical to that in Kablick et al. (2018), and performed by using a cloud-system resolving model (CSRM) which is able to resolve cloud-scale dynamic and thermodynamic processes. By resolving these processes that play a critical role in the development of clouds and their interactions with aerosols, we are able to obtain information on aerosol effects on the pyroCb development and its impacts the UTLS water vapor and cirrus clouds, and on associated dynamic and thermodynamic mechanisms. This information is likely to be more confident than that from a model that does not resolve but parameterize those cloud-scale processes. The basic modeling methodology in this study is similar to that used by Kablick et al. (2018). However, this study uses a more sophisticated microphysical scheme, i.e., a bin scheme, rather than the two-moment bulk scheme used by Kablick et al. (2018). Through extensive comparisons between various types of bin schemes and bulk schemes, Fan et al. (2012) and Khain et al. (2015) have concluded that the use of bin schemes is desirable for reasonable simulations of clouds, precipitation, and their interactions with aerosols. This is because the bin scheme explicitly predicts cloud-particle size distributions, while the bulk scheme prescribes those size distributions. The bin scheme also uses collection efficiencies and terminal velocities varying with varying cloud-particle sizes to emulate this variation in reality, while the bulk scheme in general uses fixed efficiencies and terminal velocities, which are not able to consider the variation of collection efficiencies and terminal velocities in reality. This makes the bin scheme more sophisticated than the bulk scheme.

Note that Kablick et al. (2018) examined aerosol effects on the convective development of a specific pyroCb case study, simulating microphysical conditions, detrained water vapor mixing ratios, and cirrus cloud properties only considering a typical updraft framework. The present study expands upon that work by performing sensitivity simulations in which typical updrafts in the pyroCb are allowed to vary, enabling us to ascertain the dependence of those aerosol effects on typical updrafts. Note that CAPE, which determines typical updrafts in convective clouds, are strongly dependent on surface latent and sensible heat fluxes (e.g., Houze, 1993), and in the case of pyroCb these fluxes

149 are controlled by fire intensity. Hence, these sensitivity simulations in turn enable us to
150 study the dependence of those aerosol effects on fire intensity. Here, we see that the
151 pyroCb typical updrafts are controlled by fire intensity and thus the pyroCb typical updrafts
152 are referred to as fire-driven updrafts, henceforth.
153 Aerosol effects on clouds are initiated by an increase in aerosol concentration, which
154 can be caused by an increase in aerosol emission at and near the surface, and dependent on
155 how much aerosol concentration increases, or on the magnitude of an increase in aerosol
156 concentration, i.e., aerosol perturbation (e.g., Rosenfeld et al., 2008; Koren et al., 2012).
157 This dependence has not been examined in Kablick et al. (2018) and this study examines
158 this dependence by performing additional sensitivity simulations where the magnitude of
159 aerosol perturbation varies.
160
161 **2. Modeling framework**
162
163 We use the Advanced Research Weather Research and Forecasting (ARW) model, a
164 nonhydrostatic compressible model, as the CSRM. Prognostic microphysical variables are
165 transported with a fifth-order monotonic advection scheme (Wang et al., 2009). Shortwave
166 and longwave radiation parameterizations have been included in all simulations by
167 adopting the Rapid Radiation Transfer Model (RRTM; Mlawer et al., 1997; Fouquart and
168 Bonnel, 1980).
169 To represent the microphysical processes, the CSRM adopts a bin scheme based on the
170 Hebrew University Cloud Model described by Khain et al. (2009). The bin scheme solves
171 a system of kinetic equations for the size distribution functions of water drops, ice crystals
172 (plate, columnar and branch types), snow aggregates, graupel and hail, as well as cloud
173 condensation nuclei (CCN) and ice nuclei (IN). Each size distribution is represented by 33
174 mass doubling bins, i.e., the mass of a particle m_k in the kth bin is determined as $m_k =$
175 $2m_{k-1}$.
176 The cloud-droplet nucleation parameterization, which is based on Köhler theory, is
177 used to represent cloud-droplet nucleation. Arbitrary aerosol mixing states and arbitrary
178 aerosol size distributions can be fed to this parameterization. To represent heterogeneous
179 ice-crystal nucleation, the parameterizations by Lohmann and Diehl (2006) and Möhler et

al. (2006) are used. In these parameterizations, contact, immersion, condensation-freezing, and deposition nucleation paths are all considered by taking into account the size distribution of IN, temperature and supersaturation. Homogeneous aerosol (or haze particle) and droplet freezing, based on the size distribution of droplets, is also considered following the theory developed by Koop et al. (2000).

3. Case description and simulations

3.1 Control run

The control run for an observed pyroCb case is performed over a forested site in the Canadian Northwest Territories (60.03° N, 115.45° W). Kablick et al. (2018) give details about the site and the pyroCb case. The control run is identical to the Full Simulation in Kablick et al. (2018) except for the different microphysical schemes between them; remember that this study uses a bin scheme, while Kablick et al. (2018) used a bulk scheme. The control run is performed for one day from 12:00 GMT on August 5th to 12:00 GMT on August 6th in 2014 and captures the initial, mature, and decaying stages of the pyroCb. Balloon soundings of winds, temperature and dew-point temperature were obtained every 6 hours from Ft. Smith observation station, which is located near the forested site, as described in Kablick et al. (2018). The sounding data at 12:00 GMT on August 5th are used to prescribe the initial atmospheric condition. Using the sequential soundings, at each altitude, temperature and humidity tendencies are obtained. These tendencies represent the impacts of synoptic- or large-scale motion on temperature and humidity with the assumption that sounding data represent the synoptic conditions, following Grabowski et al. (1996), Krueger et al. (1999) and Lee et al. (2018). These tendencies are horizontally homogeneous and applied to the control run every time step by interpolation. The control run is performed in a three dimensional domain with horizontal and vertical lengths of 300 km and 20 km, respectively. For the simulation, the horizontal resolution is 500 m and the vertical resolution is 200 m to resolve cloud dynamic and thermodynamic processes.

Figure 1 shows a satellite image of the observed pyroCb and the fire spot whose spatial length is ~ 40 km when it is about to advance into its mature stage. To emulate this in the

simulation, at the center of the simulation domain, a fire spot with a diameter of 40 km is placed (Figure 2). In the fire spot, the surface latent and sensible heat fluxes are set at 1800 and 15000 W m^{-2}, respectively. In areas outside of the fire spot in the domain, the surface latent and sensible heat fluxes are set at 310 and 150 W m^{-2}, respectively. These surface heat-flux values follow the previous studies which are Trentmann et al. (2006) and Luderer et al. (2006) and adopt boreal forest emissions. Following Kablick et al. (2018), the surface heat-flux values are prescribed with no temporal variation and no consideration of interactions between heat fluxes and the atmosphere in the control run. Hence, the setup for the surface heat fluxes is idealized and this enables a better isolation of aerosol effects themselves on the pyroCb development and its impacts on the UTLS water vapor and cirrus clouds for the given surface heat fluxes by excluding effects of interactions between the surface heat fluxes and atmosphere on those development and impacts.

For the selected pyroCb case, aerosol properties that can be represented by aerosol chemical composition, size distribution and concentration are unknown. Hence, in the fire spot for the first time step, the concentration of aerosols acting as CCN is prescribed to be 15000 cm^{-3} in the planetary boundary layer (PBL), and decreases exponentially with height above the PBL top. Outside of the fire spot for the first time step, the concentration of aerosols acting as CCN is prescribed to be 150 cm^{-3} in the PBL and also decreases exponentially with height above this layer. These prescribed concentrations of aerosols are typically observed in fire spots and their background (Pruppacher and Klett, 1997; Seinfeld and Pandis, 1998; Reid et al., 1999; Andreae et al., 2004; Reid et al., 2005; Luderer et al., 2009).

For the control run, the other aerosol properties are assumed to follow typical values determined in previous studies. For example, Reid et al. (2005) have shown that aerosol mass produced by forest fires is generally composed of ~50-70% of organic-carbon (OC) compounds, ~5-10% of black-carbon (BC) material, and ~20-45% of inorganic species. Based on those results, the approximate median value of each chemical component percentage range is used in the control run. Aerosol particles are assumed to be composed of 60% OC, 8% BC, and 32% inorganic species. In the control run, OC is assumed to be water soluble and composed of (by mass) 18 % levoglucosan ($C_6H_{10}O_5$, density = 1600 kg m^{-3}, van't Hoff factor = 1), 41 % succinic acid ($C_4H_6O_4$, density = 1572 kg m^{-3}, van't

Hoff factor = 3), and 41 % fulvic acid ($C_{33}H_{32}O_{19}$, density = 1500 kg m^{-3}, van't Hoff factor = 5) based on typically observed chemical composition of OC compounds over fire sites (Reid et al., 2005). In the control run, the inorganic species is assumed to be ammonium sulfate, a representative inorganic species associated with fires (Reid et al., 2005). This chemical composition taken for aerosol particles is assumed to be spatiotemporally unvarying in the control run. According to Reid et al. (2005), Knobelspiessel et al. (2011), and Lee et al. (2014), it is reasonable to assume that the initial aerosol size distribution follows the unimodal lognormal distribution in fire sites. Hence, the control run adopts the unimodal lognormal distribution as an initial aerosol size distribution. Those studies have indicated that in general, median aerosol diameter and standard deviation of the distribution range from ~0.01 to ~0.03 μm and from ~2.0 to ~2.2, respectively, for aerosols that act as CCN. By taking the approximate median value of each of these ranges, median aerosol diameter and standard deviation of the adopted unimodal distribution of aerosols as CCN are assumed to be 0.02 μm and 2.1, respectively, for the control run. Following Seinfeld and Pandis (2006) and Phillips et al. (2007), for aerosols that act as IN, median aerosol diameter and standard deviation of the unimodal distribution are assumed to be 0.1 μm and 1.6 that are typical values in the continent. For the control run, aerosol properties of IN and CCN are assumed to be identical except that at the first time step, median aerosol diameter and standard deviation of the size distribution between IN and CCN are different, and the IN concentration is 100 times lower than the CCN concentration based on a general difference in concentration between CCN and IN (Pruppacher and Klett, 1978). Aerosols are diffused and advected by air flow in clouds. After activation or captured by precipitating hydrometeors, aerosols are transported within hydrometeors and removed from the atmosphere once hydrometeors that contain aerosols reach the surface. It is assumed that in non-cloudy areas, aerosol size and spatial distributions are set to follow the background counterparts which are set at the first time step. In other words, once clouds disappear completely at any grid points, aerosol size distribution and number concentration at those points recover to the background counterparts. This assumption has been used by numerous CSRM studies and proven to simulate overall aerosol properties and their impacts on clouds and precipitation reasonably well (Morrison and Grabowski, 2011; Lebo and Morrison, 2014; Lee et al., 2016). This

assumption means that a situation where fire continuously produces aerosols to maintain the initial background aerosol concentrations is adopted by this study.

The observed cirrus cloud at the top of the pyroCb is located to the northeast of the fire spot due to the northeastward winds at the altitude of the cirrus cloud (Figure 1). The cloud first formed around the fire spot. However, winds advected it northeastward. The extent of the observed cirrus cloud is ~100 km. Figure 2 shows the simulated field of cloud-ice mass density at a time that corresponds to the satellite image in Figure 1. This field in Figure 2 represents the simulated cirrus cloud in the control run. As observed, the simulated cirrus is located to the northeast of the fire spot and the extent of the simulated cirrus cloud is ~ 100 km. Hence, we see that there is good agreement in the morphology of the cirrus cloud between the observation and the simulation.

The averaged liquid-water path (LWP) over areas with non-zero LWP in the control run is 960 g m^{-2}, while the averaged ice-water path (IWP) over areas with non-zero IWP in the control run is 202 g m^{-2}. These simulated LWP and IWP are ~10 % different from the satellite-retrieved counterparts. In this study, for the calculation of LWP (IWP), we only considered droplets (ice crystals); drops with radii smaller (greater) than 20 μm are classified as droplets (raindrops). Stated differently, droplet mass but not rain mass is used to obtain liquid-water content (LWC) and LWP, and the mass of ice crystals but not the mass of snow aggregates, graupel and hail is used to obtain ice-water content (IWC) and IWP. The averaged cloud-top height and cloud-base height over the period between when the pyroCb forms and when the pyroCb disappears is 10.3 km and 3.6 km in the control run, respectively, and these simulated top and base heights are ~7% different from the satellite-retrieved counterparts. This indicates the overall cloud macro-physical structures, as represented by LWP, IWP, cloud-top and cloud-base heights, are simulated reasonably well as compared to the observation.

The details of the reflectivity field are given in Kablick et al. (2018). There is good agreement between observed and simulated cloud reflectivity fields for this study (Figure 3). The agreement in the observed and simulated cirrus cloud, cloud macro-physical and reflectivity fields demonstrates that the pyroCb-case simulation is reasonable.

3.2 Low-aerosol run

To see the role played by fire-generated aerosols in the development of the pyroCb and its effects on water vapor and cirrus clouds in the UTLS, we repeat the control run by reducing aerosol concentration in the fire spot from 15000 cm^{-3} to the background aerosol concentration (i.e., 150 cm^{-3}). This reduction removes fire-generated aerosols in the fire spot. The only difference is in aerosol concentration in the fire spot and there are no other differences in the simulation setup which is described in Section 3.1 between the control run and this repeated run. Hence, comparisons between the control run and this repeated run, which is referred to as the low-aerosol run, will identify the role played by fire-generated aerosols in the pyroCb development and its impacts on the UTLS water vapor and cirrus clouds. Here, the low-aerosol run is identical to the Low Aerosol Simulation in Kablick et al. (2018) except for the different microphysical schemes between them.

3.3 Additional runs

We examine the above-mentioned potential variation of effects of fire-generated aerosols on the pyroCb development and its impacts on the UTLS water vapor and cirrus clouds with varying fire intensity and associated fire-driven updrafts. For the examination, we repeat the control run by varying fire intensity. Remember that surface latent and sensible heat fluxes on which fire-driven updrafts in convective clouds are strongly dependent are controlled by fire intensity. Hence, the variation of fire intensity can be represented by the variation of fire-induced surface latent and sensible heat fluxes. As a first step, the control run is repeated by reducing fire-induced surface latent and sensible heat fluxes by factors of 2 and 4. The first repeated run represents a case with medium fire intensity, while the second repeated run represents a case with weak fire intensity. Relative to these repeated runs, the control run represents a case with strong fire intensity. Henceforth, the first repeated run is referred to as “the medium run” and the second repeated run is referred to as “the weak run”. Then, to see effects of fire-generated aerosols on the pyroCb development and its impacts on the UTLS water vapor and cirrus clouds for each of those cases with different fire intensity, the medium run and the weak run are repeated with the identical initial aerosol concentration to that in the low-aerosol run. The repeated medium

run and weak run are referred to as “the medium-low run” and “the weak-low run”, respectively. The control run, the medium run, and the weak run are the polluted-scenario runs, while the low-aerosol run, the medium-low run, and the weak-low run are the clean-scenario runs. Comparisons between the medium run and the medium-low run and those between the weak run and the weak-low run isolate those effects of fire-generated aerosols for the case of medium fire intensity and the case of weak fire intensity, respectively. Comparisons between the control run and the low-aerosol run identify those aerosol effects for the case of strong fire intensity.

Effects of fire-generated aerosols on the pyroCb development and its impacts on the UTLS water vapor and cirrus clouds can also be dependent on the magnitude of fire-induced increases in aerosol concentrations or aerosol perturbation in a fire spot. Motivated by this, the previously described simulations are repeated by varying the magnitude of aerosol perturbation in the fire spot. To test the sensitivity of results to the magnitude of fire-induced aerosol perturbation, for each fire intensity, we repeat the polluted-scenario run by increasing and reducing the magnitude by a factor of 2 in the fire spot but not outside of the fire spot. These simulations with the increased magnitude have an aerosol concentration of 30000 cm^{-3} at the first time step over the fire spot in the PBL and are referred to as the control-30000 run, the medium-30000 run, and the weak-30000 run for strong, medium, and weak fire intensity, respectively. These simulations with the reduced magnitude have an aerosol concentration of 7500 cm^{-3} at the first time step over the fire spot in the PBL and are referred to as the control-7500 run, the medium-7500 run, and the weak-7500 run for strong, medium, and weak fire intensity, respectively. Motivated by the analysis described in Section 4.3, we additionally repeat the medium run and the weak run with aerosol concentrations of 2000 and 1000 cm^{-3} at the first time step over the fire spot in the PBL, respectively. The repeated medium (weak) run is referred to as the medium-2000 (the weak-1000) run. Table 1 summarizes the simulations.

The aerosol concentration of 30000 cm^{-3} over the fire spot corresponds to a situation when fire produces a larger concentration of aerosols than a typically observed range between 10000 and 20000 cm^{-3}, while the aerosol concentrations of 7500, 2000 and 1000 cm^{-3} over the fire spot corresponds to a situation when fire produces a lower concentration

of aerosols than the typically observed range (Reid et al, 1999; Andreae et al, 2004; Reid et al, 2005; Luderer et al., 2009).

4. Results

4.1 The control run and the low-aerosol run

Results from the control run and the low-aerosol run, which are equivalent to the Full Simulation and the Low Aerosol Simulation in Kablick et al. (2018), respectively, are described here. Kablick et al. (2018) mainly focused on comparisons themselves between aerosol effects and heat-flux effects on pyroCb development and its impacts on the UTLS water vapor and cirrus clouds. In this study, we expand upon the results of Kablick et al. (2018) by focusing on aerosol effects on pyroCb development and its subsequent impacts on the UTLS water vapor and cirrus clouds.

The updraft mass flux is one of the most representative variables that are indicative of the cloud dynamic intensity and the magnitude of convective invigoration. The updraft mass flux is averaged over the simulation period between 17:00 GMT on August 5th and 12:00 GMT on August 6th, and 17:00 GMT on August 5th is a time around which the pyroCb starts to from (Figure 4).

Regarding the UTLS, in this study, the upper troposphere is defined to be between ~ 9 km in altitude and the tropopause that is ~ 13 km in altitude; the equilibrium level where the buoyancy of a rising air parcel becomes zero above the level of free convection is considered to be the tropopause (Emanuel, 1994). Hence, the defined upper troposphere occupies around a quarter of the total vertical extent of the troposphere. The lower stratosphere is defined to be between the tropopause and an altitude which is 10 km above the tropopause. Hence, the UTLS is between ~9 km and ~23 km in this study. Considering that the stratosphere is between the tropopause and its top that is generally ~ 50 km in altitude, the defined lower stratosphere occupies around a quarter of the total vertical extent of the stratosphere.

Updraft mass fluxes in the control run are only ~3% greater than those in the low-aerosol run (Figure 4 and Table 2). Given the hundredfold difference in aerosol loading over the fire spot between the runs, this 3% difference in updraft fluxes is negligibly small. The comparison between water-vapor mass density over the cloudy columns and that over non-cloudy columns in the control run demonstrates that there is a substantial increase in the amount of water vapor in a part of UTLS at and above the tropopause due to the pyroCb (Figure 5 and Table 2). There is about five times greater water-vapor mass over the cloudy columns that represent the pyroCb area than in the background outside the pyroCb area in the control run. Henceforth, the UTLS water vapor means water vapor in a part of the UTLS at and above the tropopause.

Updrafts in the pyroCb transport water vapor to the UTLS at and above the tropopause, which leads to the substantial increase in the amount of the UTLS water vapor over the pyroCb area. For the simulation period between 17:00 GMT on August 5th and 12:00 GMT on August 6th, the averaged water-vapor mass fluxes at the tropopause over cloudy and non-cloudy grid columns are 8.30×10^{-6} and 0.57×10^{-6} kg m^{-2} s^{-1}, respectively. Due to the presence of the pyroCb and associated updrafts in cloudy grid columns, there are substantial increases in water vapor fluxes at the tropopause over those cloudy grid columns as compared to those fluxes in the background over non-cloudy grid columns. This leads to the larger amount of the UTLS water vapor over the pyroCb than in the background outside the pyroCb or the pyroCb area in the control run. It is also shown that the vertical extent of water vapor is extended further up to ~ 16 km by the pyroCb as compared to the extent of ~14 km in the background (Figure 5). This means that air parcels that include water vapor and rise from below the tropopause overshoot the tropopause by ~ 3 km in the pyroCb, while those parcels in the background do so by ~ 1 km. This in turn implies that air parcels and associated updrafts in the pyroCb are stronger to reach higher altitudes before their demise in the stratosphere than those in the background. Those stronger air parcels enable water-vapor layers to be deepened in the lower stratosphere, which in turn enable the interception of longwave radiation by water vapor to occur over longer paths in the lower stratosphere. These longer paths and greater water-vapor mass over the paths both contribute to more interception of longwave radiation by water vapor in the UTLS over the pyroCb than in the background.

Similar to the situation with updraft mass fluxes, there is only a small (~2%) increase in the averaged mass of the UTLS water vapor in the control run as compared to that in the low-aerosol run for strong fire intensity (Figure 5 and Table 2). The small variation in updraft mass fluxes between the control run and the low-aerosol run results in a small variation in the transportation of water vapor to the UTLS at and above the tropopause, and the averaged water-vapor fluxes at the tropopause between these two simulations. These averaged fluxes are over cloudy columns for the simulation period between 17:00 GMT on August 5th and 12:00 GMT on August 6th. The averaged water-vapor fluxes vary from 8.30×10^{-6} kg m^{-2} s^{-1} in the control run to 8.21×10^{-6} kg m^{-2} s^{-1} in the low-aerosol run.

The altitude of homogeneous freezing is at 9 km , so cirrus clouds which are composed of ice crystals (or cloud ice) only are between 9 km and 13 km. Between 9 km and 13 km, there are the presence of cloud ice and thus cirrus clouds in the control run, meaning that the pyroCb, which is simulated in the control run, produces cirrus clouds (Figure 6). The amount of cirrus clouds in the control run, as represented by the averaged cloud-ice mass density, ranges from 0.028 to 0.037 g m^{-3} between 9 km and 13 km (Figure 6). The averaged cloud-ice number concentration and cloud-ice size, as represented by its volume mean radius, between 9 km and 13 km ranges from 6 to 20 cm^{-3}, and from 10 to 20 micron, respectively. The altitudes between 9 km and 13 km correspond to a part of the UTLS below the troposphere. Henceforth, the UTLS cirrus clouds mean those clouds in a part of the UTLS below the tropopause.

Updrafts in the pyroCb produce supersaturation, which leads to the generation of cloud-ice mass and associated cirrus clouds via deposition, the primary source of cloud-ice mass. Similar to the situation with updraft mass fluxes, comparisons between the control run and the low-aerosol run for strong fire intensity show that there is only a small increase (~4%) in the mass of the UTLS circus clouds in the control run as compared to that in the low-aerosol run (Figure 6 and Table 2). However, mainly due to the larger aerosol concentrations, and associated greater homogeneous aerosol and droplet freezing, there is a large ~20-fold increase in cloud-ice number concentration and associated with this, there is a large ~2-fold decrease in cloud-ice size in the control run between 9 km and 13 km as compared to that in the low-aerosol run. Due to the negligible variation of updraft mass fluxes, there are negligible variations of supersaturation and deposition between the

simulations (Figure 7), and thus a negligible variation of the mass of the UTLS cirrus clouds between the control run and the low-aerosol run. Mainly due to the variation of aerosol concentrations, there are significant variations of cloud-ice number concentration and size between the control run and the low-aerosol run.

In summary, the pyroCb and associated updrafts cause a substantial enhancement of the transportation of water vapor to the UTLS at and above the tropopause. They also produce cirrus clouds. The role, which is played by fire-generated aerosols and their effects on the pyroCb and its updrafts, in the enhancement of the transportation of water vapor to the UTLS at and above the tropopause, and in the production of the mass of the UTLS cirrus clouds is not significant for strong fire intensity.

4.2 Dependence of aerosol effects on fire intensity

Taking interest in the negligible sensitivity of updrafts and their impacts on the UTLS water vapor and the mass of the UTLS cirrus clouds to aerosol loading in the pyroCb, we raise a possibility that this sensitivity is affected by fire intensity. When fire-generated surface heat fluxes and fire intensity are increased, it is likely that in-cloud latent heat is also increased because a major source of in-cloud latent heating is surface heat flux. Therefore, the aerosol-induced perturbations of latent heating may be relatively small compared with large in-cloud latent heat contributed by surface fluxes with very intense burning. Thus, aerosol-induced increases in parcel buoyancy, updrafts and their impacts on water vapor and the amount of cirrus clouds are relatively small compared with the large buoyancy, strong fire-driven updrafts, produced by strong fire intensity and the associated large in-cloud latent heat, and their impacts on water vapor and the amount of cirrus clouds.

Considering that a major source of in-cloud latent heat is surface heat fluxes, when the fire-generated surface heat fluxes and the fire intensity are reduced, in-cloud latent heat is also likely to be smaller. Here, we are interested in how the magnitude of an aerosol-induced perturbation of latent heating for a pyroCb with weak fire intensity is compared to that with strong fire intensity. This is to evaluate the possibility that with background in-cloud latent heat varying with fire intensity, the relative magnitude of aerosol-induced perturbation of latent heat to surface flux-dominated latent heat may vary.

4.2.1 Effects of Updrafts on the UTLS water vapor and cirrus clouds

The average updraft mass fluxes in the low-aerosol run, the medium-low run and the weak-low run as shown in Figure 4 represent fire-driven updrafts for strong, medium and weak fire intensity, respectively. Due to different fire intensity and associated CAPE, fire-driven updrafts vary between these runs. The variation of these fluxes between the clean-scenario run and the polluted-scenario run for each fire intensity is induced by fire-generated aerosols. All of the cases of weak, medium and strong fire intensity show aerosol-induced increases in updraft mass fluxes (Figure 4 and Table 2). Of interest is that the greatest percentage increase in updraft mass flux is in the case of weak fire (weak-low to weak runs), smallest in the case of strong fire (low-aerosol to control runs), and intermediate in the case of medium fire (medium-low to medium runs) (Figure 4 and Table 2). Since the updrafts mass flux is updraft speed that is multiplied by air density, and air density at each altitude does vary negligibly among simulations, differences in updraft mass fluxes are mostly explained by those in updraft speed. Hence, it can be said that percentage differences in updraft mass fluxes mean percentage differences in updraft speed with good confidence. Here, the percentage difference, including both the percentage increase and decrease, is the relative difference in the value of variables between the polluted-scenario run than the clean-scenario run for each fire intensity. This percentage difference for strong fire intensity is obtained as follows in this study:

$$\frac{The\ control\ run\ minus\ the\ low-aerosol\ run}{The\ low-aerosol\ \ run} \times 100\ (\%) \qquad (1)$$

The percentage difference for medium (weak) fire intensity is obtained by replacing the control run with the medium (weak) run, and the low-aerosol run with the medium-low (weak-low) run in Equation (1). Associated with the greater increases in updraft mass fluxes, the percentage increases in the UTLS water vapor and cloud-ice mass (Equation 1) are greater in the case of weaker fire (Figures 5 and 6 and Table 2).

In this section, we see that although fire-produced aerosols invigorate updrafts in in all three types of fire intensity, the invigoration-induced increases in the UTLS water vapor and cloud-ice mass gets larger as fire intensity weakens.

4.2.2 Volume mean radius of droplets (R_v)

a. Cloud droplet number concentration (CDNC) and LWC

The simulation period is divided into four sub-periods for this next analysis: period 1 (initial formation of the pyroCb) between 17:00 and 19:00 GMT on August 5th, period 2 between 19:00 and 21:00 GMT on August 5th, and period 3 between 21:00 GMT and 23:00 GMT on August 5th (initial stages of cloud development), and period 4 between 23:00 GMT on August 5th and 12:00 GMT on August 6th (mature and decaying stages). CDNC, which is averaged at all altitudes in cloudy areas and over period 1, decreases as the fire intensity and updrafts decrease (Figure 8). The control run, the medium run and the weak run have higher aerosol concentrations over the fire spot (Table 1), which lead to the much higher averaged CDNC than the low-aerosol run, the medium-low run, and the weak-low run, respectively. Increasing CDNC enhances competition among droplets for a given amount of water, which is available for the condensational growth of droplets, in a cloud. Enhanced competition eventually curbs the condensational growth and reduces droplet size, which is represented by R_v in this study. This explains why R_v, which is averaged at all altitudes in cloudy areas and over period 1, is smaller in the polluted-scenario run than in the clean-scenario run for each fire intensity (Figure 8). Of interest is that as fire intensity weakens, although the averaged CDNC reduces, which tends to lower the competition among droplets, the averaged R_v decreases not only among the polluted-scenario runs over the fire spot but also among the clean-scenario runs over the fire spot (Figure 8). This is because R_v is proportional to $(\frac{LWC}{CDNC})^{\frac{1}{3}}$. Here, LWC represents the given amount of water which is available for the condensational growth of droplets. This proportionality means that for a given CDNC, a decrease in LWC also causes R_v to decrease, i. e., a decrease in the available amount of water for the condensational growth with no changes in CDNC induces a decrease in R_v. LWC, which is averaged at all altitudes in cloudy areas and over period 1, also decreases with weakening fire intensity and updrafts not only among the polluted-scenario runs but also among the clean-scenario runs (Figure 8). Effects of LWC on R_v outweigh those of CDNC and this leads to the decrease in the averaged R_v with weakening fire intensity (Figure 8).

549 Using the averaged LWC and the averaged CDNC that are shown in Figure 8, it is
550 found that $(\frac{LWC}{CDNC})^{\frac{1}{3}}$ varies by 1.50×10^{-5} kg from 3.50×10^{-5} kg in the control run for strong
551 fire intensity to 2.00×10^{-5} kg in the weak run for weak fire intensity, while it varies by
552 9.80×10^{-6} kg from 1.03×10^{-4} kg in the low-aerosol run for strong fire intensity to 9.32×10^{-5}
553 kg in the weak-low run for weak fire intensity. Associated with this, the averaged R_v
554 shows a 47 % reduction from 3.20 μm in the control run to 1.70 μm in the weak run, and
555 the averaged R_v shows a 10 % reduction from 7.75 μm in the low-aerosol run to 6.98 μm
556 in the weak-low run during period 1 (Figure 8).
557 In summary, the simulated LWC, CDNC, their variation with varying fire intensity,
558 and the functional relation between LWC, CDNC and R_v , which is $R_v \propto (\frac{LWC}{CDNC})^{\frac{1}{3}}$, leads to
559 a situation where R_v reduce much more among the polluted-scenario runs than among the
560 clean-scenario runs during the period with the initial formation of the pyroCb.
561
562 **b. Equilibrium supersaturation**
563
564 During period 1, as fire intensity weakens and updraft speed decreases, parcel equilibrium
565 supersaturation, which is supersaturation when supersaturation in a rising air parcel stops
566 to increase (Rogers and Yau, 1991), lowers and thus, the minimum size of activated aerosol
567 particles increases not only among the clean-scenario runs but also among the polluted-
568 scenario runs. Mostly due to greater aerosol concentrations, the averaged equilibrium
569 supersaturation and the averaged associated minimum size of activated aerosol particles
570 over areas with positive updraft speed and period 1, are lower and higher, respectively, in
571 the polluted-scenario run than in the clean-scenario run for each fire intensity. Rogers and
572 Yau (1991) have also shown that higher aerosol concentrations induce lower and higher
573 equilibrium supersaturation and the averaged associated minimum size of activated aerosol
574 particles, respectively.
575 The averaged equilibrium supersaturation reduces from 0.21% in the control run for
576 strong fire intensity to 0.10% in the weak run for weak fire intensity. Associated with this,
577 the averaged minimum size in diameter increases from 0.09 μm in the control run to 0.12
578 μm in the weak run over period 1. The averaged equilibrium supersaturation reduces from

579 0.55% in the low-aerosol run for strong fire intensity to 0.31% in the weak-low run for
580 weak fire intensity. Associated with this, the averaged minimum size increases from 0.04
581 μm in the low-aerosol run to 0.07 μm in the weak-low run over period 1.

582 The increase in the minimum-activation size with weakening fire intensity occurs
583 closer to the right tail of the assumed unimodal aerosol size distribution among the
584 polluted-scenario runs than among the clean-scenario runs. A smaller portion of the total
585 aerosol concentration is in the size range which is closer to the right tail of the assumed
586 unimodal aerosol size distribution than that which is less close to the right tail as long as
587 changes in the minimum size in these two size ranges are similar and these ranges are on
588 the right-hand side of the aerosol distribution; most of aerosol activation occurs for aerosol
589 sizes on the right-hand side of the distribution peak, here we are only concerned with the
590 size ranges on the right-hand side. So, a similar increase in the averaged minimum-
591 activation size for a weakened fire results in a smaller percentage reduction in the total
592 activated aerosol concentration and thus CDNC among the polluted-scenario runs than
593 among the clean-scenario runs during period 1. CDNC, which is averaged in cloudy areas
594 and period 1, decreases by 8% from 850 cm^{-3} in the control run to 780 cm^{-3} in the weak
595 run. The averaged CDNC decreases by 76% from 33 cm^{-3} in the low-aerosol run to 8 cm^{-3}
596 in the weak-low run (Figure 8). This contributes to greater reduction in $(\frac{LWC}{CDNC})^{\frac{1}{3}}$ and thus
597 R_v as fire intensity weakens among the polluted-scenario runs than among the clean-
598 scenario runs during period 1. This is for a similar simulated LWC between the polluted-
599 scenario run and the clean-scenario run for each fire intensity (Figure 8).

600 In summary, due to larger aerosol concentrations and associated lower equilibrium
601 supersaturation, the variation of the number of activated aerosols with varying fire intensity
602 and updrafts occurs in the aerosol size range that is closer to the right tail of the assumed
603 aerosol size distribution in the polluted-scenario runs than in the clean-scenario runs. In
604 the size range that is closer to the right tail of the size distribution, there is a smaller portion
605 of aerosol concentrations and thus the smaller percentage variation of the number of
606 activated aerosols and CDNC in the polluted-scenario runs than in the clean-scenario runs.
607 This smaller variation of CDNC aids the greater reduction in R_v among the polluted-
608 scenario runs than among the clean-scenario runs via the relation of $R_v \propto (\frac{LWC}{CDNC})^{\frac{1}{3}}$, in the

situation where LWC is similar between the polluted-scenario run and the clean-scenario run for each fire intensity.

4.2.3 Autoconversion, freezing, deposition and condensation

According to previous studies (e.g., Khairoutdinov and Kogan, 2000; Liu and Daum, 2004; Lee and Baik, 2017), autoconversion is proportional to the size of cloud droplets. This is explained by the fact that the efficiency of collection among droplets is proportional to droplet size (Pruppacher and Klett, 1978; Rogers and Yau, 1991). Due to the larger R_v during period 1, the subsequent autoconversion rates, which are averaged in cloudy areas and over period 2, are higher in the clean-scenario run than in the polluted-scenario run for each fire intensity (Figure 9a). Due to the larger absolute and percentage reduction in R_v, as described in Section 4.2.2, there is a larger absolute and percentage reduction in autoconversion rate among the polluted-scenario runs than among the clean-scenario runs with weakening fire intensity during period 2 (Figure 9a). The averaged autoconversion rates over period 2 reduce from 3.61×10^{-6} g m^{-3} s^{-1} in the control run with strong fire intensity to 0.93×10^{-6} g m^{-3} s^{-1} in the weak run with weak fire intensity through 2.01×10^{-6} g m^{-3} s^{-1} in the medium run with medium fire intensity by 74%. Those averaged autoconversion rates reduce from 4.52×10^{-6} g m^{-3} s^{-1} in the low-aerosol run with strong fire intensity to 3.94×10^{-6} g m^{-3} s^{-1} in the weak-low run with weak fire intensity through 4.43×10^{-6} g m^{-3} s^{-1} in the medium-low run with medium fire intensity by 14%. Associated with this, differences in the averaged autoconversion rates between the polluted-scenario run and the clean-scenario run get greater as fire intensity weakens during period 2 (Figure 9a).

Due to smaller autoconversion rates, there is more cloud liquid available for freezing in the polluted-scenario run than in the clean-scenario run for each fire intensity, particularly during period 2. Hence, the rate of cloud-liquid freezing, which is averaged in cloudy areas and period 2, is greater in the polluted-scenario run than in the clean-scenario run for each fire intensity (Figure 9a). Differences in autoconversion rates between the polluted-scenario run and the clean-scenario run, which increase with weakening fire intensity, induce those differences in the amount of cloud liquid available for freezing to

get greater with weakening fire intensity (Figure 9a). Thus, differences in the averaged rate of cloud-liquid freezing between the polluted-scenario run and the clean-scenario run over period 2 gets greater with weakening fire intensity (Figure 9a). Due to this, differences in freezing-related latent heat between the runs increase with weakening fire intensity. When fire intensity is strong, the difference in freezing-related latent heat, which is averaged in cloudy areas and period 2, between the polluted-scenario run, which is the control run, and the clean-scenario run, which is the low-aerosol run, is 1.60×10^{-4} J m^{-3} s^{-1}. However, with medium fire intensity, that difference between the polluted-scenario run, which is the medium run, and the clean-scenario run, which is the medium-low run, is 6.98×10^{-4} J m^{-3} s^{-1}, while with weak fire intensity, that difference between the polluted-scenario run, which is the weak run, and the clean-scenario run, which is the weak-low run, is 7.94×10^{-4} J m^{-3} s^{-1}. This corresponds to the variation of the percentage differences, which are calculated by Equation (1), in the averaged freezing-related latent heat between the polluted-scenario run and the clean-scenario run from 9% with strong fire intensity to 83% with weak fire intensity through 51% with medium fire intensity over the period 2.

As shown in Lee et al. (2017), enhanced freezing-related latent heat strengthens updrafts in places where freezing occurs and this, in turn, enhances deposition and deposition-related latent heat. Hence, although deposition, which is averaged in cloudy areas and period 2, is slightly lower, due to those strengthened updrafts, the averaged deposition and deposition-related latent heat are greater in the polluted-scenario run than in the clean-scenario run for each fire intensity during period 3 (Figures 9a and 9b). Differences in the averaged freezing rate (and thus the averaged freezing-related latent heating) in cloudy areas between the polluted-scenario run and the clean-scenario run for each fire intensity do not change much up to ~20:30 GMT after they start to appear around 18:30 GMT (Figure 10). However, after ~20:30 GMT, these differences start to increase as time goes by for each fire intensity. This is because as convection intensifies, the transportation of cloud liquid to places above the freezing level starts to be effective around 20:30 GMT.

The greater freezing and thus freezing-related latent heat in the polluted-scenario run than in the clean-scenario run for each fire intensity, which start to be significant around 20:30 GMT as compared to those before 20:30 GMT, invigorates updrafts, which are

represented by the averaged updraft mass fluxes in cloud areas. This subsequently causes updrafts to be stronger in the polluted-scenario run than in the clean-scenario run for each fire intensity from ~21:00 GMT on (Figure 10). Then, the stronger updrafts induce deposition, which is averaged in cloudy areas, to be greater in the polluted-scenario run than in the clean-scenario run for each fire intensity. This is around 10-20 minutes after the stronger updrafts in the polluted-scenario run than in the clean-scenario run for each fire intensity start to occur (Figure 10). Note that deposition-related latent heat is about one order of magnitude greater than freezing-related latent heat for a unit of mass of hydrometeors involved in phase-transition processes. This contributes to much greater differences in deposition-related latent heat during period 3 than those in freezing-related latent heat between the polluted-scenario run and the clean-scenario run for each fire intensity during period 2 or 3 (Figures 9a and 9b).

To satisfy mass conservation, the enhanced updrafts above the freezing level, due to enhanced freezing and deposition, induce more updraft mass fluxes below the freezing level in polluted-scenario run than in the clean-scenario run for each fire intensity. This leads to more convergence around and below cloud base, which is air flow from environment to cloud, in the polluted-scenario run than in the clean-scenario run for each fire intensity. The more mass fluxes and the more convergence below the freezing level, in turn, enhance condensation. Hence, condensation, which is averaged in cloud areas, starts to be greater when time reaches ~22:30 GMT in the polluted-scenario run than in the clean-scenario run for each fire intensity (Figure 10). This induces the averaged condensation and condensation-related latent heat to be greater in the polluted-scenario run than in the clean-scenario run for each fire intensity during period 4 (Figure 9c). Enhanced condensation in turn enhances updrafts, establishing a positive feedback between freezing, deposition, condensation, and updrafts and thus, enhancing freezing, deposition, condensation, and updrafts further. This enhancement due to feedback eventually determines the overall differences in the pyroCb properties and their impacts on the UTLS water vapor and cloud ice between the polluted-scenario run than in the clean-scenario run for each fire intensity.

Differences in freezing-related latent heat between the polluted-scenario run and the clean-scenario run increase with weakening fire intensity, particularly during period 2.

Thus, percentage differences in freezing-affected updrafts and subsequently in deposition-related latent heat, which is averaged in cloudy areas and over period 3, between the polluted-scenario run and the clean-scenario run also increase with weakening fire intensity (Figures 9a, 9b and 10). Those differences, as calculated by Equation (1), in deposition-related latent heat are 16%, 181%, and 417 % for strong, medium, and weak fire intensity, respectively (Figures 9b and 10). Since percentage increases in deposition-related latent heat in the polluted-scenario run get greater with weakening fire intensity, the subsequent percentage increases in updrafts in the polluted-scenario run as compared to updrafts in the clean-scenario run get greater with weakening fire intensity, particularly during period 3 (Figure 10). During period 4, due to these greater increases in updrafts in the polluted-scenario run with weaker fire intensity, the percentage increases in condensation in the polluted-scenario run as compared to condensation in the clean-scenario run get greater with weakening fire intensity (Figures 9c and 10). Then, the increases in condensation, in turn, further enhance the increases in updrafts in the polluted-scenario run for each fire intensity. This enhancement is greater with weaker fire intensity due to the greater increases in condensation with weaker fire intensity. This leads to the greater overall effects of fire-produced aerosols on the UTLS water vapor and ice with weaker fire intensity.

In this section, we see that the smaller R_v leads to lower autoconversion rates and a larger amount of cloud liquid as a source of freezing, which in turn induce higher freezing rates and stronger feedbacks between freezing, deposition, condensation and updrafts in the polluted-scenario run than in the clean-scenario run for each fire intensity. This results in stronger updrafts and their impacts on the UTLS water vapor and ice in the polluted-scenario run than in the clean-scenario run for each fire intensity. The greater R_v reduction among the polluted-scenario runs than among the clean-scenario runs with weakening fire intensity induces the differences in autoconversion, freezing and the feedbacks between the polluted-scenario run and the clean-scenario run to get greater as fire intensity weakens. This results in the greater impacts of aerosol-induced stronger updrafts on the UTLS water vapor and ice with weaker fire intensity.

4.3 Dependence of aerosol effects on the magnitude of aerosol perturbation

Table 3 shows that for each of the strong-, medium-, and weak-fire cases, there are increases in the UTLS water-vapor mass and in the amount of the UTLS cirrus clouds in the run with the fire-induced aerosol perturbations of 30000 or 7500 cm^{-3}. These increases are relative to the mass and the amount in the low-aerosol run for the strong-fire case, in the medium-low run for the medium-fire case, and in the weak-low run for the weak-fire case, respectively, with no fire-induced aerosol perturbation. Note that for each of the three types of fire-induced aerosol perturbations of 30000, 15000 and 7500 cm^{-3}, aerosol-perturbation-induced percentage increases in the UTLS water-vapor mass and the amount of the UTLS cirrus clouds get greater as fire intensity weakens (Tables 2 and 3). The qualitative nature of results regarding the dependence of the percentage increases in the UTLS water-vapor mass and the amount of the UTLS cirrus clouds on fire intensity thus does not depend on the magnitude of the fire-induced aerosol perturbation.

Until now, we considered the situation where the fire-induced aerosol perturbation does not vary with fire intensity. Note that so far, we have taken interest in the sensitivity to fire intensity of an aerosol perturbation on pyroCb development, the UTLS water vapor, and cirrus clouds. Hence, to examine and isolate the sensitivity, we have shown comparisons among sensitivity simulations by varying only fire intensity while maintaining a constant aerosol perturbation. While working well for the isolation aspect, this strategy does not reflect reality well. It may be that weaker fire intensity produces a smaller aerosol concentration. This possibility is not that unrealistic, since stronger fire likely involves more material burnt and more aerosols from it.

With this situation in mind, we make comparisons among three pairs of simulations: the low-aerosol run and the control-30000 run for strong fire vs. the medium-low run and the medium run for medium fire vs. the weak-low run and the weak-7500 run for weak fire. Hence, among these three pairs, the magnitude of fire-induced aerosol perturbation reduces with weakening fire, emulating the possibility that weaker fire intensity involves a less amount of aerosols. For strong fire, the perturbation-related aerosol concentration is 30000 cm^{-3}, for medium fire, it is 15000 cm^{-3}, and for weak fire, it is 7500 cm^{-3}. As shown in Tables 2 and 3, comparisons among these three pairs show that relative importance of aerosol effects on the pyroCb development and its impacts on UTLS water vapor and cirrus clouds increases for weaker fires, and it does not matter if the aerosol perturbation reduces

or stays constant with weakening fire intensity. In these comparisons, it is also possible that when fire-induced aerosol perturbation is very low for medium or weak fire intensity, the latent heat perturbation by aerosol perturbation can be very low. This very low latent heat is not large enough to increase the relative importance of those aerosol effects with weakening fire intensity. Based on this, the medium run and the weak run are repeated again. The medium run is repeated with lower fire-induced aerosol perturbations than the perturbation of 15000 cm^{-3}, while the weak run is repeated with lower fire-induced aerosol perturbations than the perturbation of 7500 cm^{-3}. Recall that when the repeated medium run has the aerosol perturbation of 2000 cm^{-3}, the repeated medium run is referred to as the medium-2000 run; when the repeated weak run has the aerosol perturbation of 1000 cm^{-3}, the repeated weak run is referred to as the weak-1000 run. The percentage increases in the UTLS water vapor and cirrus-cloud amount from the medium-low run to the medium-2000 run or from the weak-low run to the weak-1000 run are smaller than those increases, for the case of strong fire, from the low-aerosol run to the control-30000 run. This indicates that when fire-induced aerosol perturbation reduces too much with weakening fire intensity, the relative importance of aerosol effects on pyroCb development and its impacts on the UTLS water vapor and cirrus clouds no longer increases with the weakening fire intensity.

Results in this section shows that the increasing impacts of fire-induced aerosol perturbations on the UTLS water vapor and cirrus clouds with weakening fire intensity is robust whether those aerosol perturbations vary with varying fire intensity or not, unless the variation of aerosol perturbations is extremely high.

5. Conclusions

This study investigates an observed case of a pyroCb using a modeling framework. In particular, this study focuses on effects of fire-produced aerosols on pyroCb development and its impacts on the UTLS water vapor and cirrus clouds. Results show that pyroCb updrafts transport water vapor to the tropopause and above efficiently. This leads to a much greater amount of water vapor around and above the tropopause (i.e., the UTLS) over the pyroCb as compared to that in the background outside the pyroCb. The pyroCb also generates a deck of cirrus cloud around the tropopause. It is found that the role played by

fire-produced aerosols or the fire-induced aerosol perturbation in the water-vapor transportation to UTLS and the production of cirrus cloud in the pyroCb gets more significant as fire intensity weakens.

As fire intensity weakens, due to the reduction in LWC, R_v decreases despite the reduction in CDNC that tends to increase R_v. During the initial stage, there is a similar LWC between the polluted-scenario run (i.e., the control run for strong fire intensity, the medium run for medium fire intensity and the weak run for weak fire intensity with the fire-induced aerosol perturbation) and the clean-scenario run (i.e., the low-aerosol run for strong fire intensity, the medium-low run for medium fire intensity and the weak-low run for weak fire intensity with no fire-induced aerosol perturbation) for each fire intensity. The reduction in LWC with weakening fire intensity among the polluted-scenario runs is also similar to that among the clean-scenario runs. During the initial stage, there are much greater CDNC in the polluted-scenario run than in the clean-scenario run for each fire intensity, and the smaller CDNC reduction among the polluted-scenario runs than among the clean-scenario runs with weakening fire intensity. This situation during the initial stage induces R_v to reduce much more among the polluted-scenario runs than among the clean-scenario runs with weakening fire intensity. This reduces autoconversion more among the polluted-scenario runs than among the clean-scenario runs with weakening fire intensity. This makes differences in autoconversion between the polluted-scenario run and the clean-scenario run increase as fire intensity weakens. The increasing difference in autoconversion between the polluted-scenario run and the clean-scenario run causes greater differences in freezing-related latent heat as fire intensity weakens. Through feedback between freezing, deposition, updrafts, and condensation, differences in freezing-related latent heat induce differences in updrafts between the polluted-scenario run and the clean-scenario run. Those greater differences in freezing-related latent heat also lead to greater differences in updrafts, producing the greater differences in the UTLS water vapor and cirrus clouds between the runs with weaker fire intensity. This means that the role of fire-produced aerosols in water-vapor transport to the UTLS and the production of cirrus cloud in the pyroCb becomes more significant as fire intensity weakens.

The more significant role of fire-produced aerosols in water-vapor transport to the UTLS and the production of cirrus cloud in the pyroCb with weaker fire intensity is robust

826 to the magnitude of the given fire-induced aerosol perturbation which was assumed not to
827 vary with varying fire intensity. This more significant role with weaker fire intensity is also
828 robust to the variation of the fire-induced aerosol perturbation with the varying fire
829 intensity unless the variation is very high.

830 It is true that the level of the understanding of a mechanism that controls the role
831 played by fire-produced aerosols in the development of pyroCbs and their impacts on the
832 UTLS water vapor and cirrus clouds has been low. This study shows that fire-produced
833 aerosols can invigorate convection and updrafts and thus cause enhanced transportation of
834 water vapor to the UTLS and enhanced formation of cirrus clouds. This study finds that
835 the mechanism that controls the invigoration of convection by aerosols in the pyroCb is
836 consistent with the traditional invigoration mechanism which was proposed and detailed in
837 Rosenfeld et al. (2008). However, this study shows that for pyroCbs produced by strong
838 fires, the aerosol-induced invigoration and its effects on the UTLS water vapor and cirrus
839 clouds are insignificant. Note that traditional understanding generally focuses on effects of
840 fire-produced heat and water vapor and their associated fluxes around the surface on the
841 pyroCb and does not consider effects of fire-produced aerosols on the pyroCb, and this
842 understanding adequately explains the mechanics for pyroCbs in association with strong
843 fires. However, this study suggests that the role of fire-produced aerosols in pyroCb
844 development and its effects on the UTLS water vapor and cirrus clouds should be
845 considered for cases where pyroCbs form over weak-intensity fires, should one be observed
846 in nature.

847 It is of interest to note that when fire-induced aerosol perturbations are strongly
848 reduced for cases of weaker-intensity fires compared with strong-intensity fires, the
849 significance of the role played by fire-produced aerosol perturbation does not increase any
850 longer and starts to reduce with weakening fire. This suggests that there is a critical level
851 of aerosol perturbation below which the increase in the significance with weakening fire
852 intensity ceases.

853
854
855
856

Author contributions

SSL came up with the research goals and aims, preformed the simulations, and wrote the manuscript. GK and ZL selected the case, analyzed observations, and provided data to set up the simulations while reviewing and providing comments on the manuscript. CHJ and YSC revised manuscript based on the reviewers' comments and perform associated analyses of simulation and observation data.

Acknowledgements

This study is supported by the National Aeronautics and Space Administration through grant NNX16AN61G and the National Science Foundation through grant AGS 1837811. This study was also supported by the National Strategic Project-Fine particle of the National Research Foundation of Korea (NRF) funded by the Ministry of Science and ICT (MSIT), the Ministry of Environment (ME), the Ministry of Health and Welfare (MOHW) (NRF-2017M3D8A1092022) and the ministry of Education (NRF-2018R1D1A1A09083227).

919 **References**

920

921 Albrecht, B. A.: Aerosols, cloud microphysics, and fractional cloudiness, Science, 245,
922 1227-1230, 1989.
923 Andreae, M. O., Rosenfeld, D., Artaxo, P., Costa, A. A., Frank, G. P., Longo, K. M., and
924 Silva-Dias, M. A. F.: Smoking rain clouds over the Amazon, Science, 303, 1337–1342,
925 2004.
926 Fan, J., Leung, L. R., Li, Z.: Aerosol impacts on clouds and precipitation in eastern China:
927 Results from bin and bulk microphysics, J. Geophys. Res., 117, D00K36,
928 doi:10.1029/2011JD016537, 2012.
929 Fouquart, Y., and Bonnel, B.: Computation of solar heating of the Earth's atmosphere: a
930 new parameterization, Beitr. Phys. Atmos., 53, 35-62, 1980.
931 Fromm, M., Lindsey, D. T., Servranckx, R., Yue, G., Trickl, T., Sica, R., Doucet, P., Godin-
932 Beekmann, S., et al.: The untold story of pyrocumulonimbus, B. Am. Meteorol. Soc.,
933 91, 1193, doi:10.1175/2010BAMS3004.1, 2010.
934 Grabowski, W. W., Wu, X., Moncrieff, M. W.: Cloud resolving modeling of tropical cloud
935 systems during phase III of GATE. Part I: Two-Dimensional Experiments, J. Atmos.
936 Sci., 53, 3684-3709, 1996.
937 Houze, R. A.: Cloud dynamics, Academic Press, 573 pp, 1993.
938 Kablick, G., Fromm, M., Miller, S., Partain, P., Peterson. D., Lee, S. S., Zhang, Y., Lambert,
939 A., and Li, Z.: The Great Slave Lake pyroCb of 5 August 2014: observations,
940 simulations, comparisons with regular convection, and impact on UTLS water vapor,
941 J. Geophy. Res., https://doi.org/10.1029/2018JD028965, 2018.
942 Emanuel, K.: Atmospheric convection, Oxford University Press, 580 pp, 1994.
943 Khain, A., Ovtchinnikov, M., Pinsky, M.: Notes on the state-of-the-art numerical modeling
944 of cloud microphysics, Atmos. Res., 55, 159-224, 2000.
945 Khain, A.: Notes on state-of-the-art investigations of aerosol effects on precipitation: a
946 critical review, Environ. Res. Lett., 4, doi:10.1088/1748-9326/4/1/015004, 2009.
947 Khain, A., BenMoshe, N., and Pokrovsky, A.: Factors determining the impact of aerosols
948 on surface precipitation from clouds: Attempt of classification, J. Atmos. Sci., 65,
949 1721-1748, 2008.

Khain, A. P., et al.: Representation of microphysical processes in cloud resolving models: Spectral (bin) microphysics versus bulk parameterization, Rev. Geophys., 53, 247–322, doi:10.1002/2014RG000468, 2015.

Khairoutdinov, M., and Kogan, Y.: A new cloud physics parameterization in a large-eddy simulation model of marine stratocumulus, Mon. Wea. Rev., 128, 229-243, 2000.

Knobelspiesse, K., Cairus, B., Ottaviani, M., et al.: Combined retrievals of boreal forest fire aerosol properties with a polarimeter and lidar, Atmos. Chem. Phys., 11, 7045-7067, 2011.

Koop, T., Luo, B. P, Tsias, A. and Peter, T,: Water activity as the determinant for homogeneous ice nucleation in aqueous solutions, Nature, 406, 611-614. 2000.

Koren, I., Altaratz, O., Remer, L. A., et al.: Aerosol-induced intensification of rain from the tropics to the mid-latitudes, Nat. Geosci., 5, 118-122, 2012.

Krueger, S. K., Cederwall, R. T., Xie, S. C., and Yio, J. J.: GCSS Working Group 4 Model Intercomparison-procedures for Case 3: Summer 1997 ARM SCM IOP. Draft manuscript obtainable from http://www.arm.gov/docs/scm/scmic3, 1999.

Lebo, Z. J. and Morrison, H.: Effects of horizontal and vertical grid spacing on mixing in simulated squall lines and implications for convective strength and structure, Mon. Wea. Rev., 143, 4355-4375, 2014.

Lee, H., and Baik, J.-J.: A physically based autoconversion parameterization, J. Atmos. Sci., 74, 1599-1615, 2017.

Lee, S. S., Donner, L. J., Phillips, V. T. J., and Ming, Y.: The dependence of aerosol effects on clouds and precipitation on cloud-system organization, shear and stability, J. Geophys. Res., 113, D16202, 2008.

Lee, S. S., Feingold, G., Koren, I., Yu, H., Yamaguchi, T., and McComiskey, A.: Effect of gradients in biomass burning aerosol on circulations and clouds, J. Geophys. Res., 119, 9948-9964, 2014.

Lee, S. S., Kim, B. -G., Yum, S. S., et al.: Effect of aerosol on evaporation, freezing and precipitation in a multiple cloud system, Clim. Dyn., 48, 1069-1087, 2016.

Lee, S. S., Li, Z., and Mok, J., et al.: Interactions between aerosol absorption, thermodynamics, dynamics, and microphysics and their impacts on clouds and precipitation in a multiple-cloud system, Clim. Dyn., 49, 3905-3921, 2017.

981 Lee, S. S., and Penner, J. E.: Comparison of a global-climate model to a cloud-system
982 resolving model for the long-term response of thin stratocumulus clouds to
983 preindustrial and present-day aerosol conditions, Atmos. Chem. Phys., 10, 6371-6389,
984 2010.
985 Lee, S. S., Penner, J. E., and Saleeby, S. M.: Aerosol effects on liquid-water path of thin
986 stratocumulus clouds., J. Geophys. Res., 114, D07204, 2009.
987 Liu, Y., and Daum, P. H.: Parameterization of the autoconversion process. Part I: Analytical
988 formulation of the Kessler-type parameterizations, J. Atmos. Sci., 61, 1539-1548,
989 2004.
990 Lohmann, U. and Diehl, K.: Sensitivity studies of the importance of dust ice nuclei for the
991 indirect aerosol effect on stratiform mixed-phase clouds, J. Atmos. Sci., 63, 968-982,
992 2006.
993 Luderer, G., Trentmann, J., Winterrath, T., Textor, C., Herzog, M., Graf, H., and Andreae,
994 M.: Modeling of biomass smoke injection into the lower stratosphere by a large forest
995 fire (part ii): Sensitivity studies. Atmos. Chem. Phy., 6, 5261–5277, 2006.
996 Luderer, G., Trentmann, J., and Andreae, M.: A new look at the role of fire-released
997 moisture on the dynamics of atmospheric pyro-convection, Int. J. Wildland Fire, 18,
998 554-562, 2009.
999 Mlawer, E. J., Taubman, S. J., Brown, P. D., Iacono, M. J., and Clough, S. A.: RRTM, a
1000 validated correlated-k model for the longwave, J. Geophys. Res., 102, 16663-1668,
1001 1997.
1002 Möhler, O., et al.: Efficiency of the deposition mode ice nucleation on mineral dust particles,
1003 Atmos. Chem. Phys., 6, 3007-3021, 2006.
1004 Morrison, H., and Grabowski, W. W.: Cloud-system resolving model simulations of aerosol
1005 indirect effects on tropical deep convection and its thermodynamic environment,
1006 Atmos. Chem. Phys., 11, 10503-10523, 2011.
1007 Peterson, D., Fromm, M., Solbrig, J., Hyer, E., Surratt, M., and Campbell, J.: Detection
1008 and inventory of intense pyroconvection in western North America using GOES-15
1009 daytime infrared data, J. Appl. Meteorol. Clim., 56, 471-493, 2017.
1010 Phillips, V. T. J., Donner, L. J., and Garner, S.: Nucleation processes in deep convection
1011 simulated by a cloud-system-resolving model with double-moment bulk microphysics,

1012 J. Atrmos. Sci., 64, 738-761, 2007.
1013 Pruppacher, H. R., and Klett, J. D.: Microphysics of clouds and precipitation, 714pp, Reidel
1014 D., 1978.
1015 Pumphrey, H., Santee, M., Livesey, N., Schwartz, M., and Read, W.: Microwave Limb
1016 Sounder observations of biomass-burning products from the Australian bush fires of
1017 February 2009, Atmos. Chem. Phys., 11, 6285-6296, 2011.
1018 Reid, J. S., Hobbs, P. V., Rangno, A. L., and Hegg, D. A.: Relationships between cloud
1019 droplet effective radius, liquid water content, and droplet concentration for warm
1020 clouds in Brazil embedded in biomass smoke, J. Geophys. Res., 104, 6145-6153, 1999.
1021 Reid, J. S., Koppmann, R., Eck T. F., and Eleuterio, D.: A review of biomass burning
1022 emissions part II: intensive physical properties of biomass burning particles, Atmos.
1023 Chem. Phys., 5,799-825, 2005.
1024 Rogers, R. R., and Yau, M. K.: A short course in cloud physics, Pergamon Press, 293pp,
1025 1991.
1026 Rosenfeld, D., Lohmann, U., Raga, G. B., et al.: Flood or drought, How do aerosols affect
1027 precipitation? Science, 321, 1309-1313, 2008.
1028 Seinfeld, J. H. and Pandis, S. N.: Atmospheric Chemistry and Physics: From Air Pollution
1029 to Climate Change, John Wiley & Sons, 1326 pp, 1998.
1030 Solomon, S., Rosenlof, K. H., Portmann, R. W., Daniel, J. S., Davis, S. M., Sanford, T. J.,
1031 and Plattner, G. K.: Contributions of stratospheric water vapor to decadal changes in
1032 the rate of global warming, Science, 327, 1219–1223, 2010.
1033 Storer, R. L., van den Heever, S. C., and Stephens, G. L.: Modeling aerosol impacts on
1034 convection under differing storm environments, J. Atmos. Sci., 67, 3904-3915, 2010.
1035 Tao, W.-K., Chen, J.-P., Li, Z., Wang, C., and Zhang, C.: Impact of aerosols on convective
1036 clouds and precipitation, Rev. Geophys., 50, RG2001, 2012.
1037 Trentmann, J., Luderer, G., Winterrath, T., Fromm, M., Servranckx, R., Textor, C., et al.:
1038 Modeling of biomass smoke injection into the lower stratosphere by a large forest fire
1039 (part i): reference simulation. Atmos. Chem. Phys., 6, 5247–5260, 2006.
1040 Twomey, S.: The influence of pollution on the shortwave albedo of clouds, J. Atmos. Sci.,
1041 34, 1149-1152, 1977.
1042 Wang, H., Skamarock, W. C., and Feingold, G.: Evaluation of scalar advection schemes in

the Advanced Research WRF model using large-eddy simulations of aerosol-cloud interactions, Mon. Wea. Rev., 137, 2547-2558, 2009.

FIGURE CAPTIONS

Figure 1. VIIRS visible image of the fire, smoke and cirrus cloud which are associated with the selected pyroCb. Bright white represents cirrus (anvil) at the top of the pyroCb, while the red circle marks the fire spot. Dark white represents smoke produced by the fire. Adapted from Kablick et al. (2018).

Figure 2. The simulated fire spot (red circle) and the field of cloud-ice mass density (cirrus cloud) at the top of the simulated pyroCb when the pyroCb is about to advance to its mature stage.

Figure 3. The vertical distribution of the radar reflectivity which is averaged over the Cloudsat path.

Figure 4. Vertical distributions of the averaged updraft mass fluxes at all altitudes in cloudy areas (where the sum of LWC and IWC is non-zero) over the simulation period between 17:00 GMT on August 5th and 12:00 GMT on August 6th.

Figure 5. Vertical distributions of average water-vapor mass density at altitudes above 13 km and over the simulation period between 17:00 GMT on August 5th and 12:00 GMT on August 6th. Colored lines represent the averaged values over cloudy grid columns (non-zero sum of LWP and IWP). The black line represents those values over non-cloudy columns (zero sum of LWP and IWP) in the control run.

Figure 6. Vertical distributions of the averaged cloud-ice mass density at all altitudes in cloudy areas (non-zero sum of LWC and IWC) over the simulation period between 17:00 GMT on August 5th and 12:00 GMT on August 6th.

Figure 7. Same as Figure 6 but for deposition rate.

Figure 8. The averaged CDNC, R_v, and LWC at all altitudes in cloudy areas, over the period between 17:00 and 19:00 GMT on August 5th.

Figure 9. The averaged rates of condensation, deposition and cloud-liquid freezing at all altitudes in cloudy areas and over periods (a) 2, (b) 3 and (c) 4. In panel (a), the average autoconversion rates are additionally shown.

Figure 10. Time series of differences in the average values of variables related to aerosol-induced invigoration of convection, at all altitudes in cloudy areas between the (a) control and low-aerosol runs for strong fire intensity, (b) medium and medium-low runs for medium fire intensity and (c) weak and weak-low runs for weak fire intensity.

Simulations	Surface sensible heat fluxes in the fire spot (W m^{-2})	Surface latent heat fluxes in the fire spot (W m^{-2})	Aerosol concentration in the PBL over the fire spot (cm^{-3})
Control run	15000	1800	15000
Low-aerosol run	15000	1800	150
Control-30000	15000	1800	30000
Control-7500	15000	1800	7500
Medium run	7500	900	15000
Medium-low run	7500	900	150
Medium-30000	7500	900	30000
Medium-7500	7500	900	7500
Medium-2000	7500	900	2000
Weak run	3750	450	15000
Weak-low run	3750	450	150
Weak-30000	3750	450	30000
Weak-7500	3750	450	7500
Weak-1000	3750	450	1000

Table 1. Summary of simulations

	Backg-round	Control	Low-aerosol	Differe-nce (%)	Medium	Meidum-low	Differe-nce (%)	Weak	Weak-low	Differe-nce (%)
Updraft mass fluxes (kg m^{-2} s^{-1})		1.23	1.19	3	0.89	0.70	27	0.42	0.21	100
Water-vapor mass density between 13 and 16 km (10^{-3} g m^{-3})	0.46	2.31	2.26	2	1.61	1.32	22	0.93	0.58	60
Cirrus-cloud mass density between 9 and 13 km (g m^{-3})		0.024	0.023	4	0.017	0.012	42	0.008	0.004	100

Table 2. The averaged updraft mass fluxes at all altitudes in cloudy areas, the averaged water-vapor mass density over altitudes between 13 and 16 km and over cloudy columns except for the averaged background water-vapor mass density which is also over altitudes between 13 and 16 km but over non-cloudy columns, and the averaged cirrus-cloud mass density between 9 and 13 km in cloudy areas. 16 km is an altitude to which the non-zero water-vapor mass density over cloudy columns extends (Figure 5). These averaged values are obtained over the simulation period between 17:00 GMT on August 5th and 12:00 GMT on August 6th. "Difference" is the percentage difference between the polluted-scenario run and the clean-scenario run for each fire intensity ($\frac{The\ polluted-scenario\ run\ minus\ the\ clean-scenario\ run}{The\ clean-scenario\ run} \times 100$ (%)).

	Control-30000	Control-7500	Medium-30000	Medium-7500	Medium-2000	Weak-30000	Weak-7500	Weak-1000
Water vapor mass density between 13 and 16 km (10^{-3} g m^{-3})	2.38 (5%)	2.28 (0.9%)	1.87 (42%)	1.50 (14%)	1.36 (3%)	1.31 (125%)	0.75 (29%)	0.60 (3%)
Cirrus cloud mass density between 9 and 13 km (g m^{-3})	0.025 (9%)	0.023 (0.2%)	0.023 (92%)	0.014 (17%)	0.012 (3%)	0.013 (225%)	0.006 (50%)	0.004 (8%)

Table 3. The averaged water-vapor mass density between 13 and 16 km over cloudy columns and, the averaged cirrus-cloud mass density between 9 and 13 km in cloudy areas, over the simulation period between 17:00 GMT on August 5th and 12:00 GMT on August 6th. The numbers in parentheses are the percentage differences: $\frac{The\ control-30000\ (or\ the\ control-7500)\ run\ minus\ the\ low-aerosol\ run}{The\ low-aerosol\ run} \times 100\ (\%)$ for strong fire intensity, $\frac{The\ medium-30000\ (or\ the\ medium-7500\ or\ the\ medium-2000)\ run\ minus\ the\ medium-low\ run}{The\ medium-low\ run} \times 100\ (\%)$ for medium fire intensity, and $\frac{The\ weak-30000\ (or\ the\ weak-7500\ or\ the\ weak-1000)\ run\ minus\ the\ weak-low\ run}{The\ weak-low\ run} \times 100\ (\%)$ for weak fire intensity.

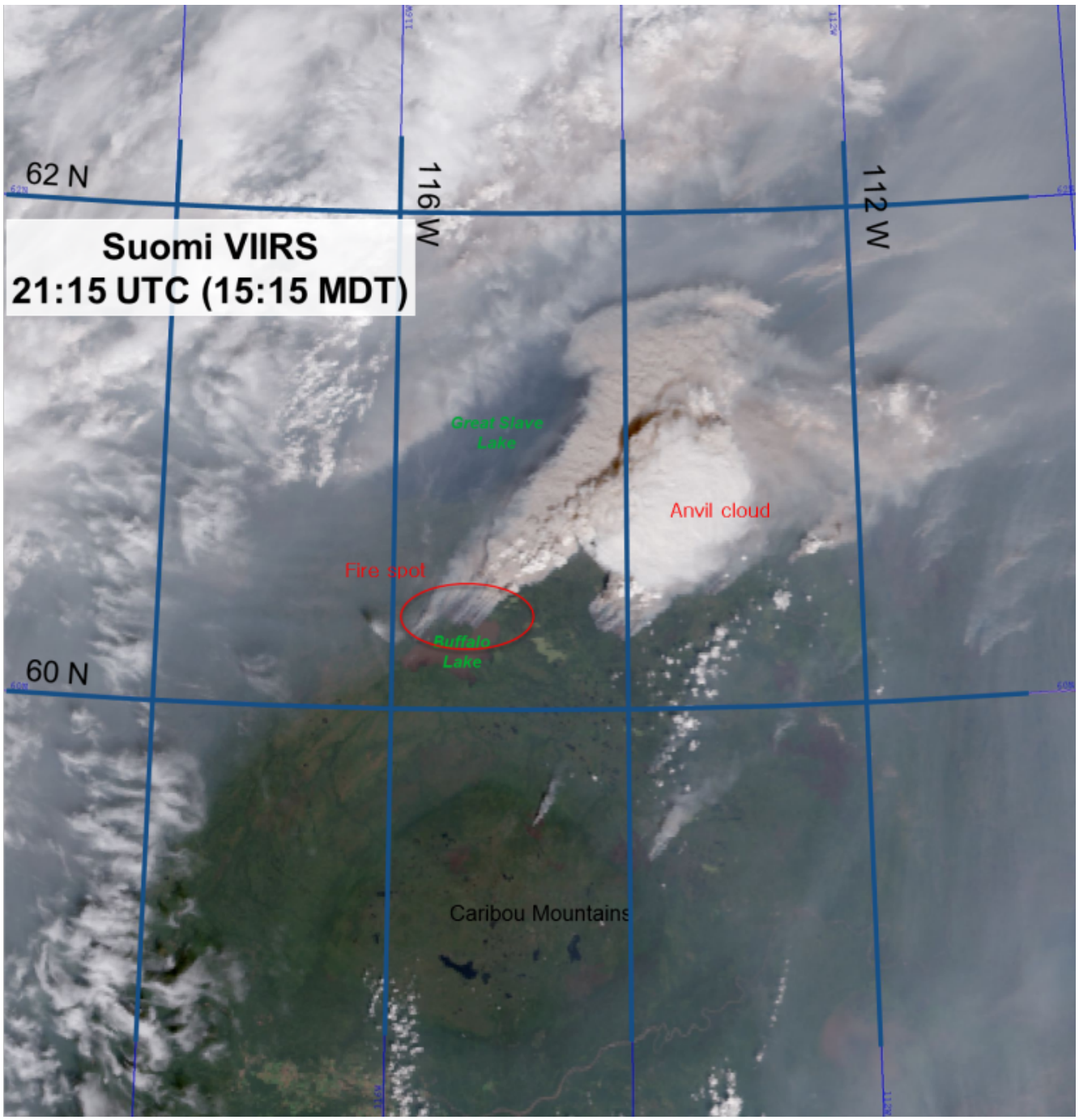
62 N
116 W
112 W
Suomi VIIRS
21:15 UTC (15:15 MDT)
Great Slave Lake
Anvil cloud
Fire spot
Buffalo Lake
60 N
Caribou Mountains

Figure 1

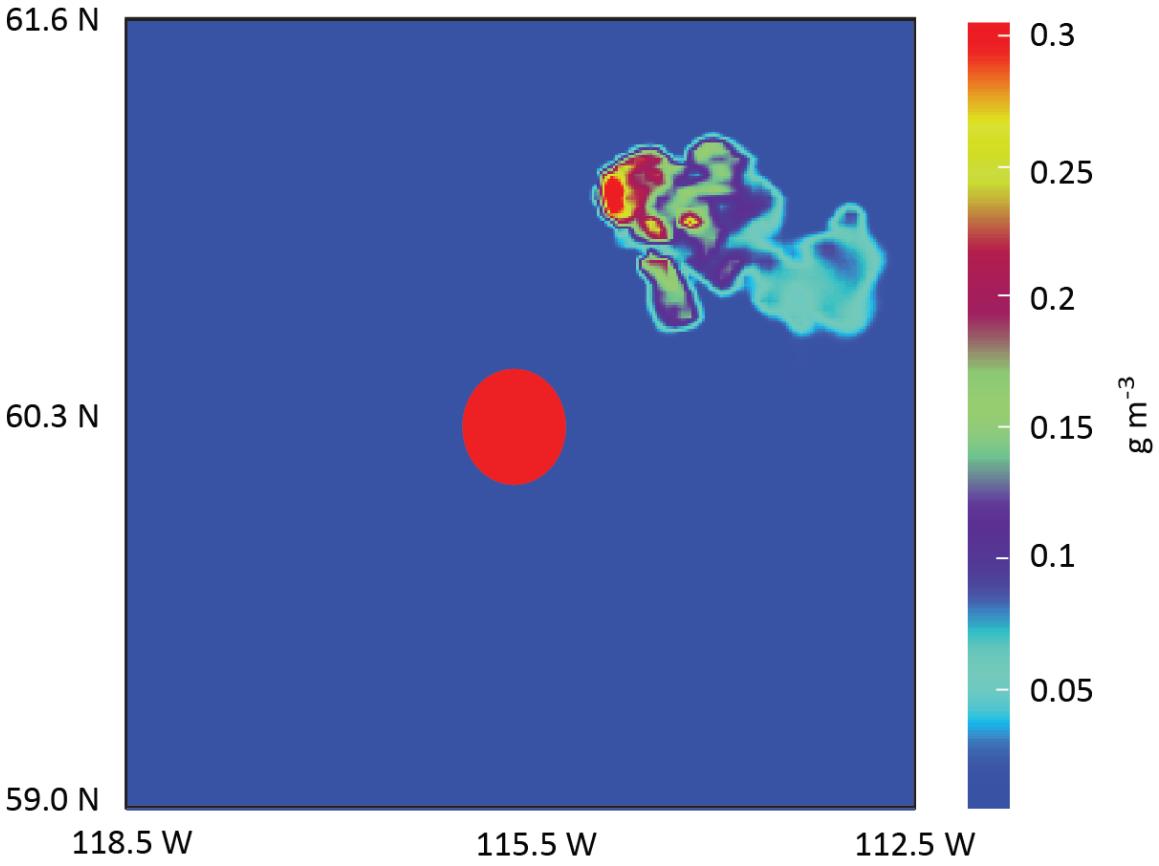

Figure 2

1213

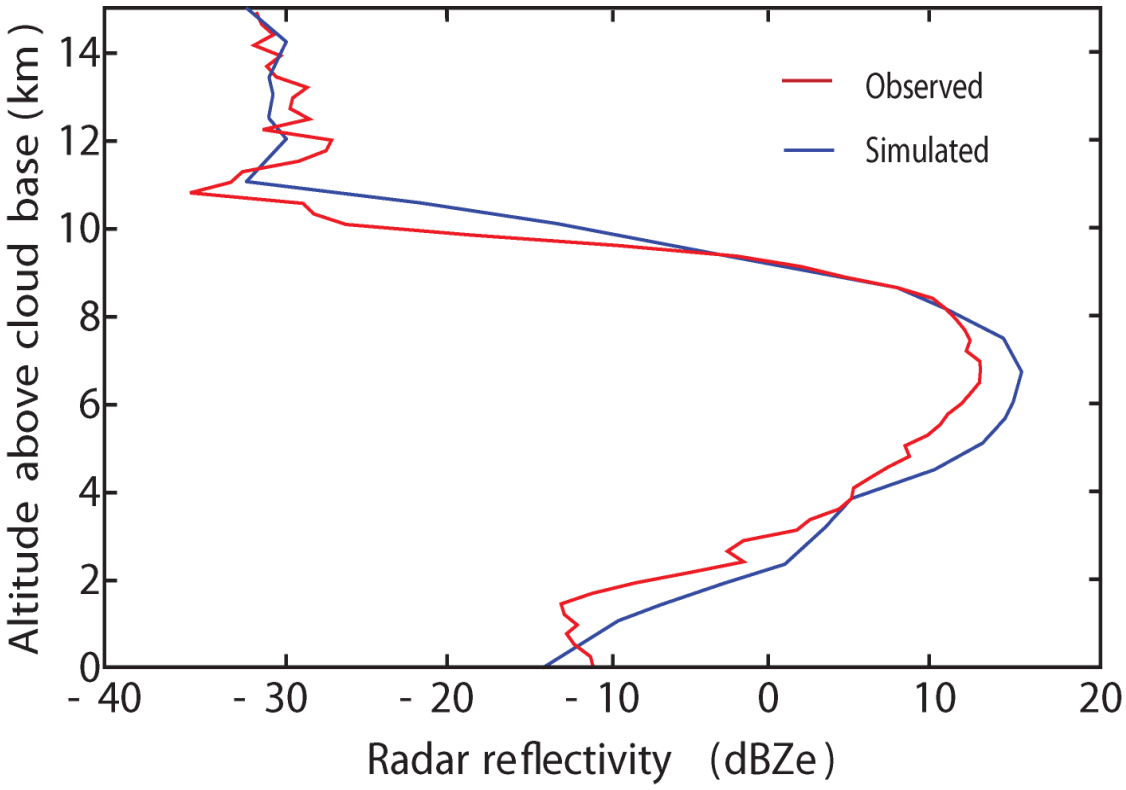

1214

1215 **Figure 3**

1216

1217

1218

1219

1220

1221

1222

1223

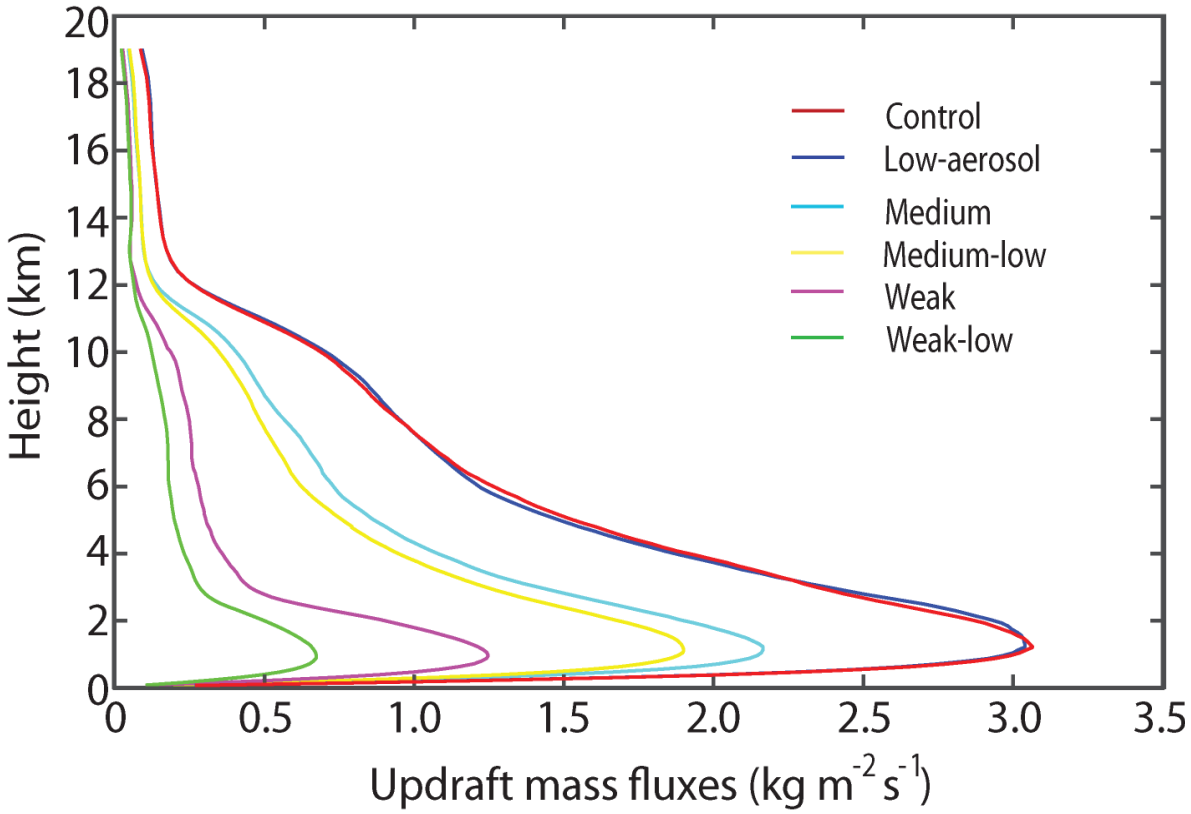
Height (km)
Updraft mass fluxes (kg m-2 s-1)
Control
Low-aerosol
Medium
Medium-low
Weak
Weak-low
0
2
4
6
8
10
12
14
16
18
20
0
0.5
1.0
1.5
2.0
2.5
3.0
3.5

Figure 4

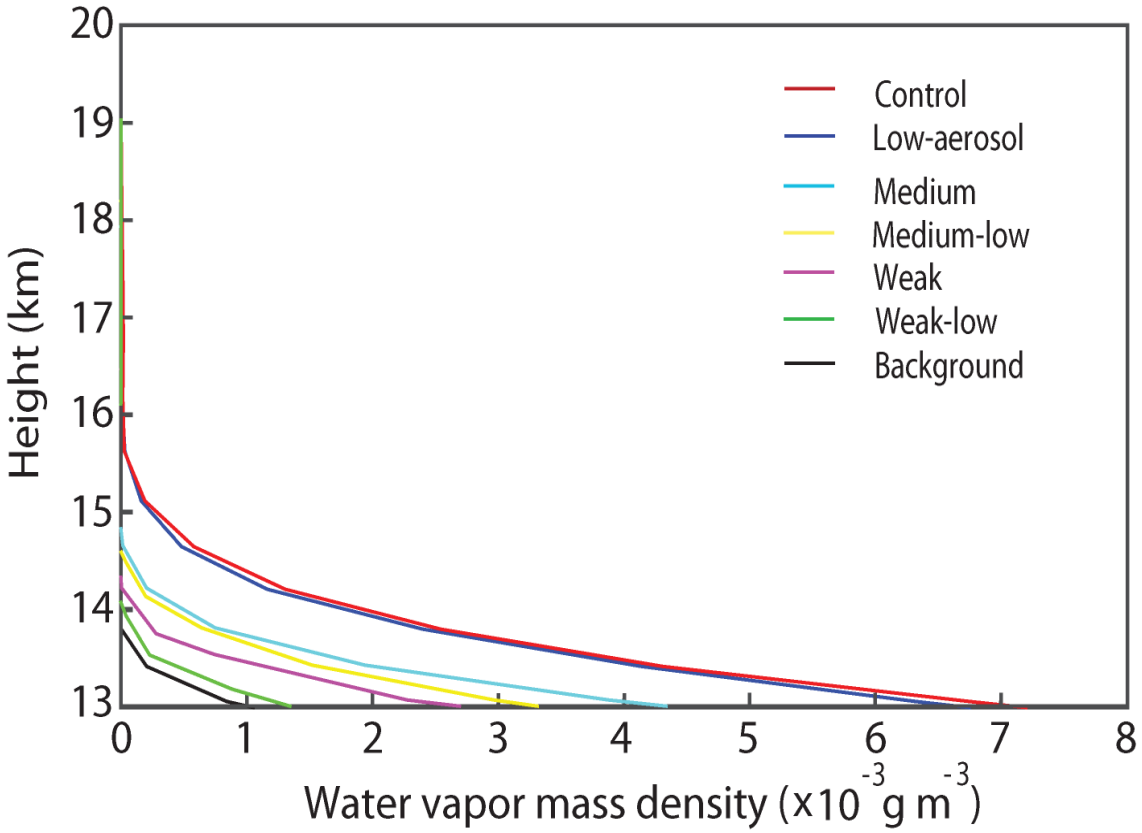
Height (km)
20
19
18
17
16
15
14
13
0
1
2
3
4
5
6
7
8
Water vapor mass density (x10 -3 g m -3)
Control
Low-aerosol
Medium
Medium-low
Weak
Weak-low
Background

Figure 5

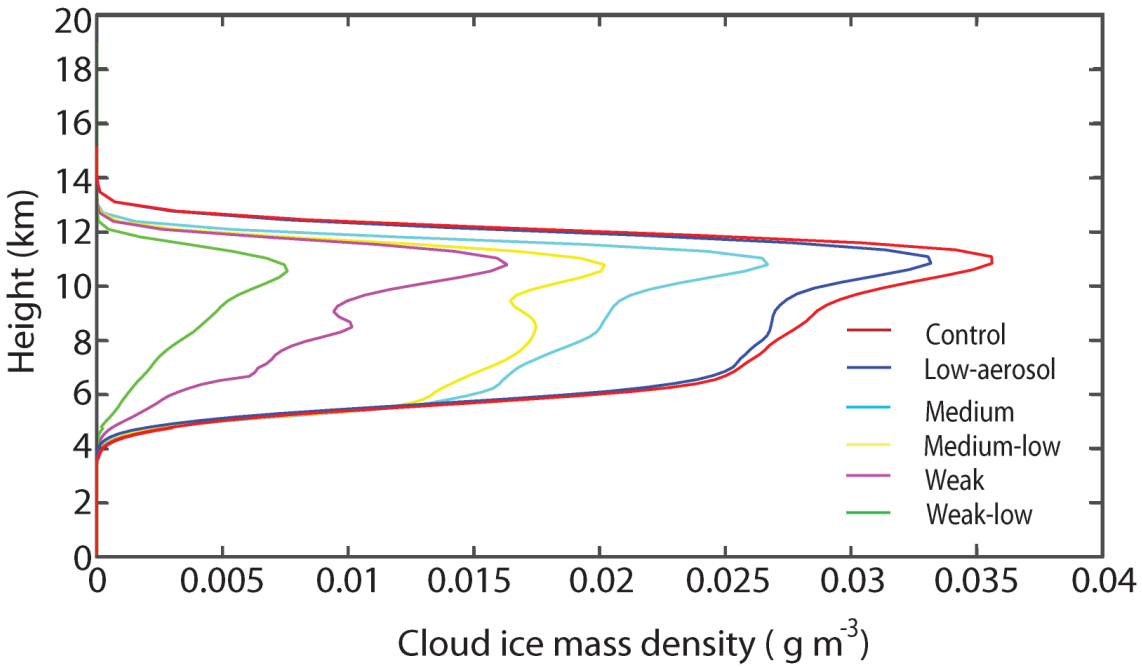

1244

1245 **Figure 6**

1246

1247

1248

1249

1250

1251

1252

1253

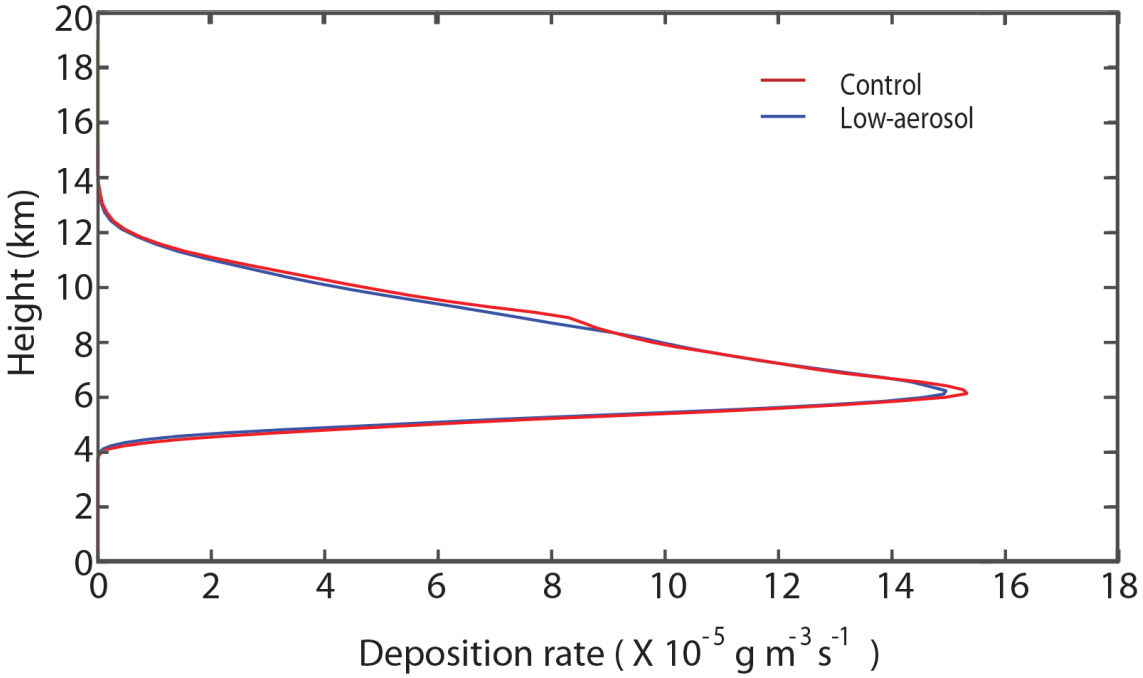
Control
Low-aerosol
Height (km)
Deposition rate (X 10-5 g m-3 s-1)
0
2
4
6
8
10
12
14
16
18
20

Figure 7

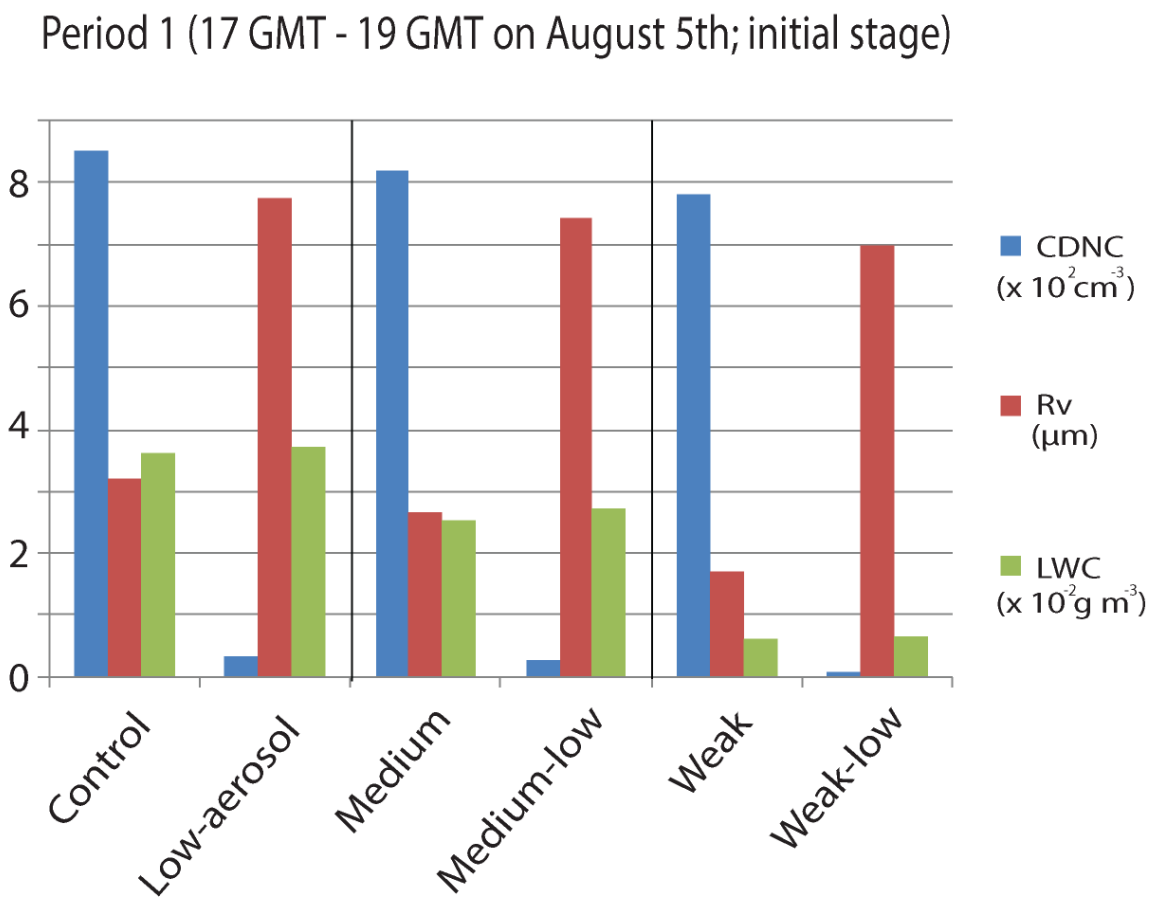
Period 1 (17 GMT - 19 GMT on August 5th; initial stage)
8
6
4
2
0
Control
Low-aerosol
Medium
Medium-low
Weak
Weak-low
CDNC
(x 10^2 cm^-3)
Rv
(µm)
LWC
(x 10^-2 g m^-3)

Figure 8

1271

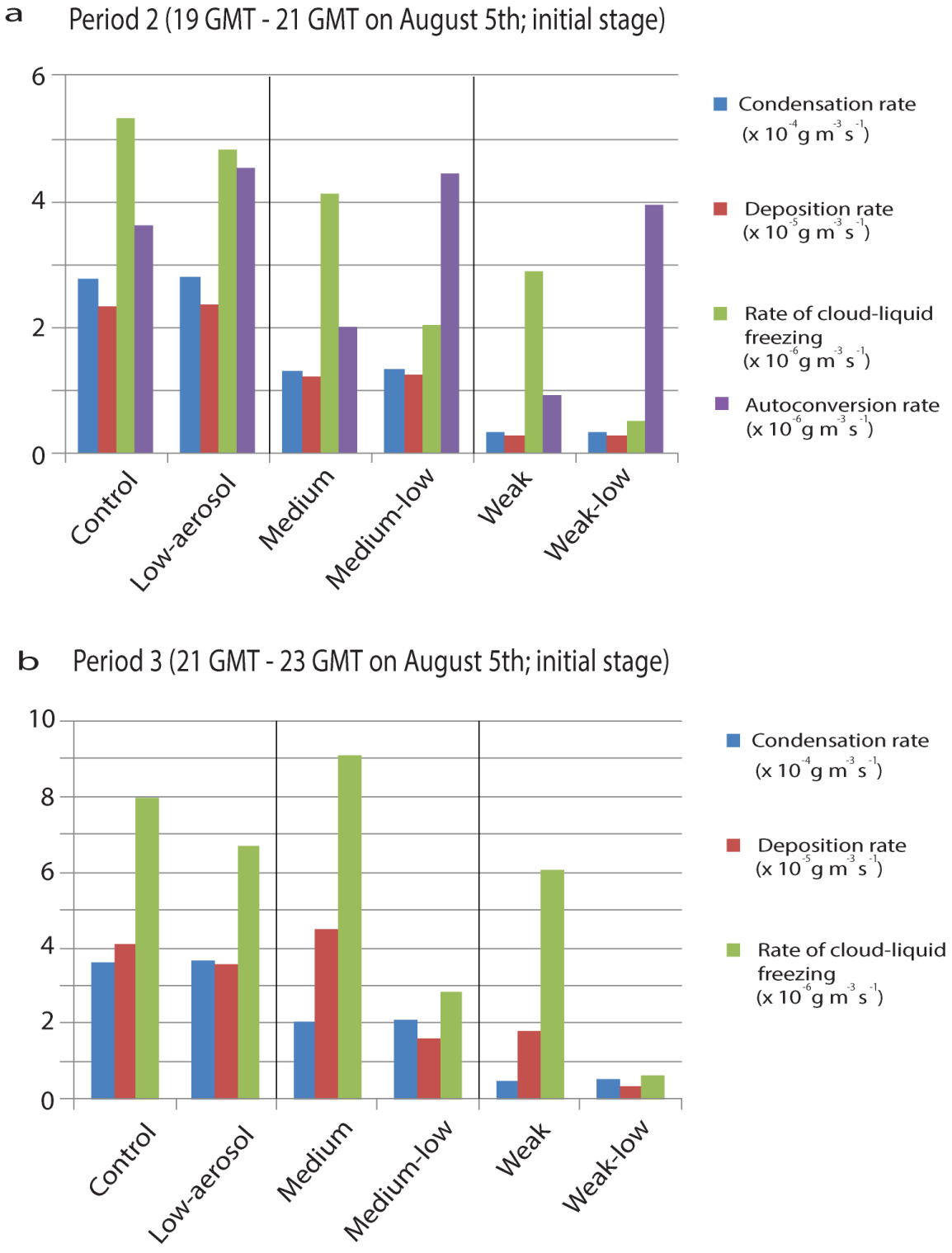

1272

1273 **Figure 9**

1274

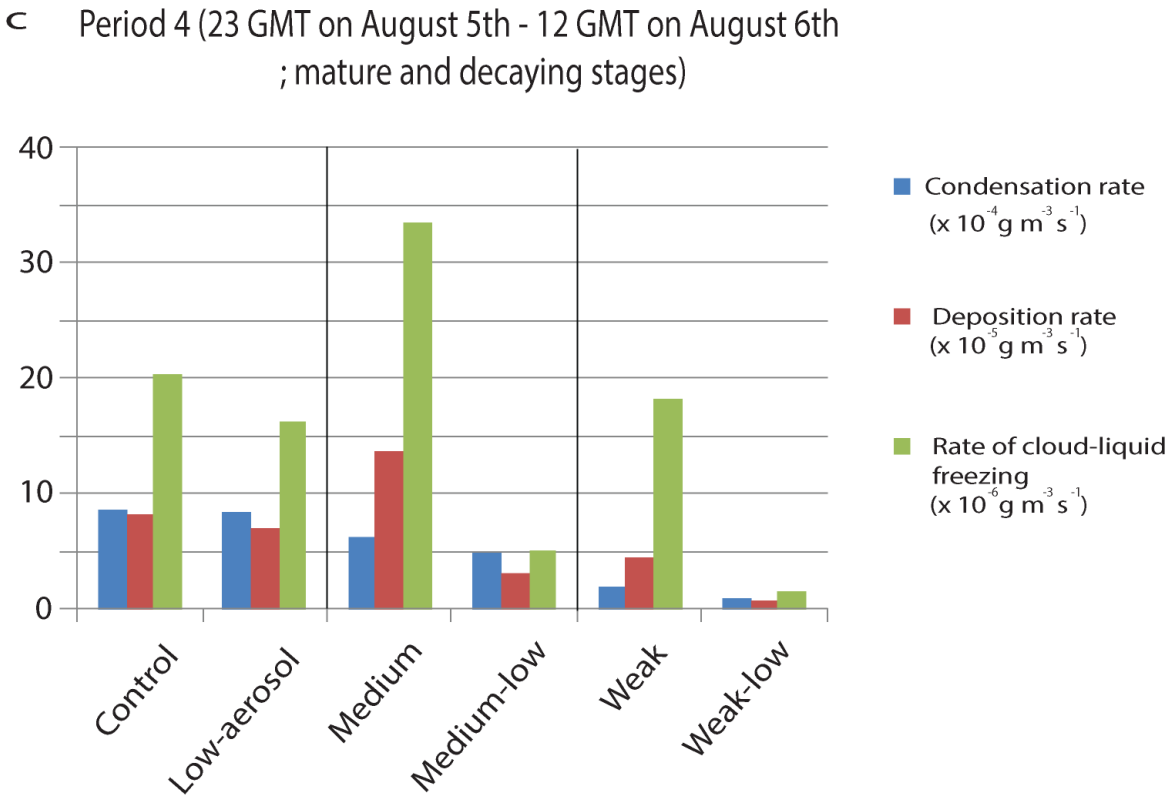

1275

1276 **Figure 9**

1277

1278

1279

1280

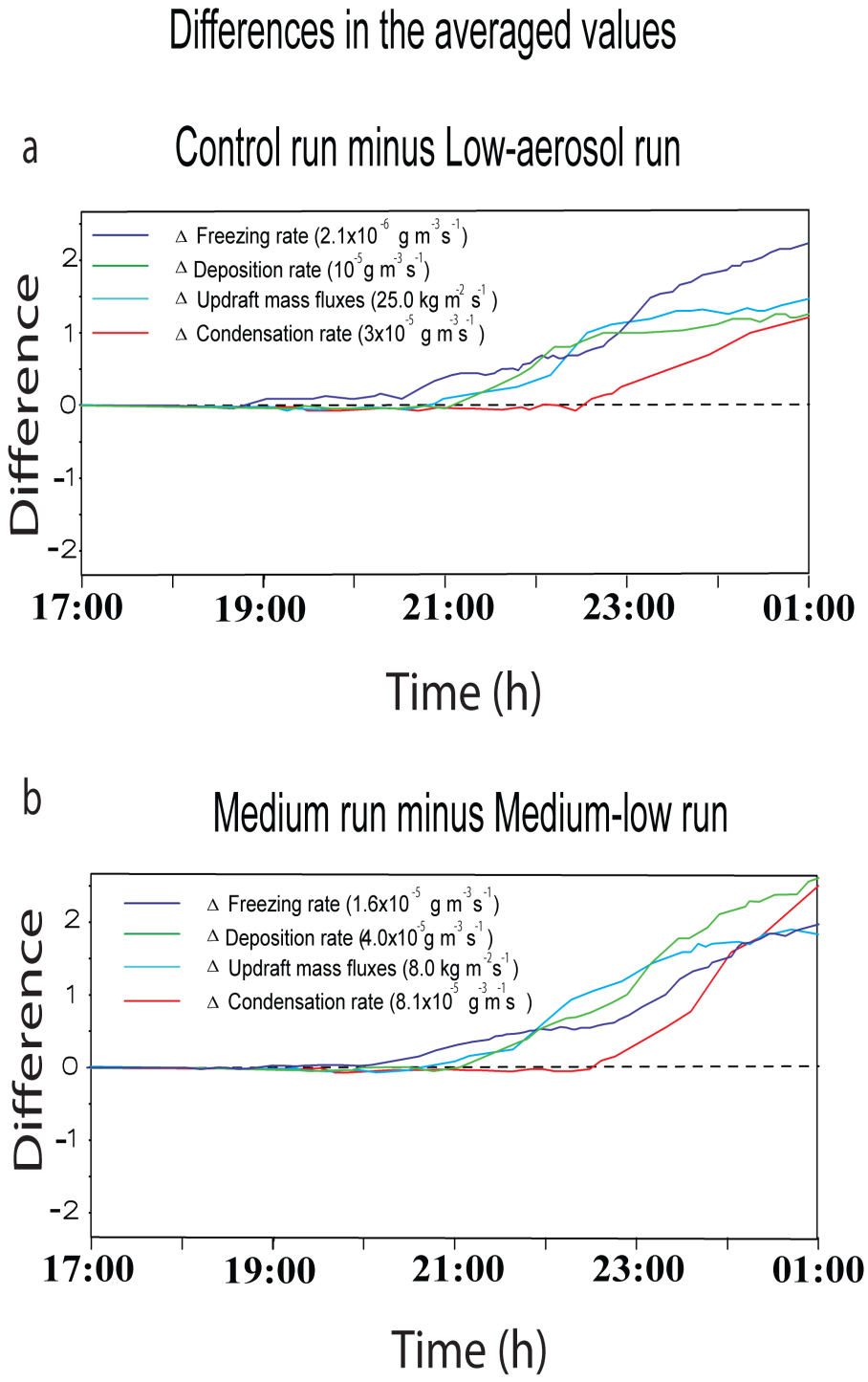

1281

1282 **Figure 10**

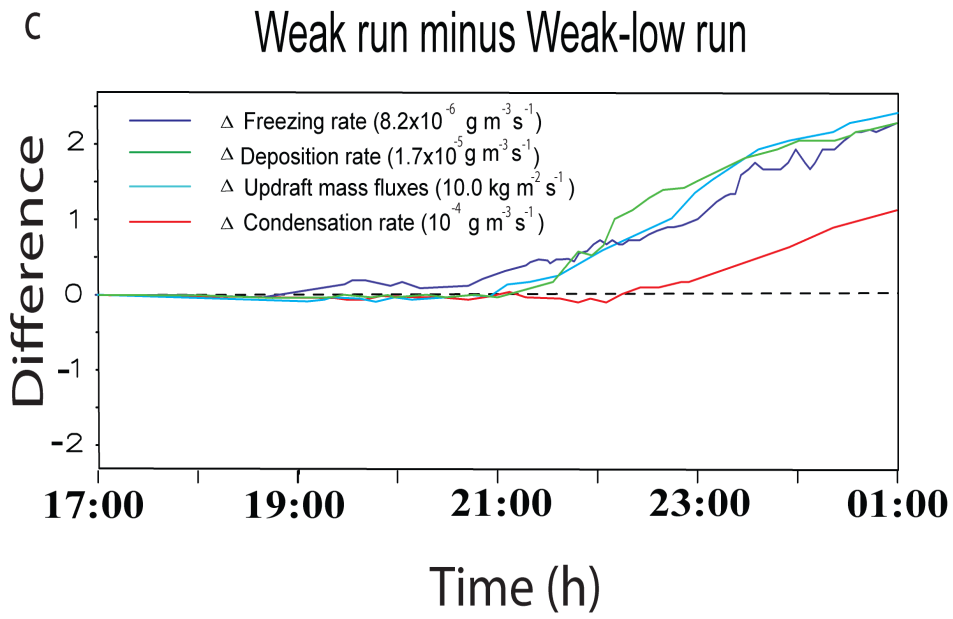
c
Weak run minus Weak-low run
Δ Freezing rate (8.2x10-6 g m-3 s-1)
Δ Deposition rate (1.7x10-5 g m-3 s-1)
Δ Updraft mass fluxes (10.0 kg m-2 s-1)
Δ Condensation rate (10-4 g m-3 s-1)
Difference
2
1
0
-1
-2
17:00
19:00
21:00
23:00
01:00
Time (h)

Figure 10